

University of Texas Rio Grande Valley

ScholarWorks @ UTRGV

Physics and Astronomy Faculty Publications
and Presentations

College of Sciences

11-20-2019

Tests of general relativity with the binary black hole signals from the LIGO-Virgo catalog GWTC-1

B. P. Abbott

Soma Mukherjee

The University of Texas Rio Grande Valley, soma.mukherjee@utrgv.edu

Follow this and additional works at: https://scholarworks.utrgv.edu/pa_fac



Part of the [Astrophysics and Astronomy Commons](#), and the [Physics Commons](#)

Recommended Citation

Abbott, B. P. and Mukherjee, Soma, "Tests of general relativity with the binary black hole signals from the LIGO-Virgo catalog GWTC-1" (2019). *Physics and Astronomy Faculty Publications and Presentations*. 12. https://scholarworks.utrgv.edu/pa_fac/12

This Article is brought to you for free and open access by the College of Sciences at ScholarWorks @ UTRGV. It has been accepted for inclusion in Physics and Astronomy Faculty Publications and Presentations by an authorized administrator of ScholarWorks @ UTRGV. For more information, please contact justin.white@utrgv.edu, william.flores01@utrgv.edu.

Tests of general relativity with the binary black hole signals from the LIGO-Virgo catalog GWTC-1

B. P. Abbott *et al.**

(The LIGO Scientific Collaboration and the Virgo Collaboration)



(Received 29 March 2019; published 20 November 2019)

The detection of gravitational waves by Advanced LIGO and Advanced Virgo provides an opportunity to test general relativity in a regime that is inaccessible to traditional astronomical observations and laboratory tests. We present four tests of the consistency of the data with binary black hole gravitational waveforms predicted by general relativity. One test subtracts the best-fit waveform from the data and checks the consistency of the residual with detector noise. The second test checks the consistency of the low- and high-frequency parts of the observed signals. The third test checks that phenomenological deviations introduced in the waveform model (including in the post-Newtonian coefficients) are consistent with 0. The fourth test constrains modifications to the propagation of gravitational waves due to a modified dispersion relation, including that from a massive graviton. We present results both for individual events and also results obtained by combining together particularly strong events from the first and second observing runs of Advanced LIGO and Advanced Virgo, as collected in the catalog GWTC-1. We do not find any inconsistency of the data with the predictions of general relativity and improve our previously presented combined constraints by factors of 1.1 to 2.5. In particular, we bound the mass of the graviton to be $m_g \leq 4.7 \times 10^{-23}$ eV/ c^2 (90% credible level), an improvement of a factor of 1.6 over our previously presented results. Additionally, we check that the four gravitational-wave events published for the first time in GWTC-1 do not lead to stronger constraints on alternative polarizations than those published previously.

DOI: [10.1103/PhysRevD.100.104036](https://doi.org/10.1103/PhysRevD.100.104036)

I. INTRODUCTION

Einstein's theory of gravity, general relativity (GR), has withstood a large number of experimental tests [1]. With the advent of gravitational-wave (GW) astronomy and the observations by the Advanced LIGO [2] and Advanced Virgo [3] detectors, a range of new tests of GR have become possible. These include both weak-field tests of the propagation of GWs, as well as tests of the strong-field regime of compact binary sources. See [4–8] for previous applications of such tests to GW data.

We report results from tests of GR on all the confident binary black hole GW events in the catalog GWTC-1 [9], i.e., those from the first and second observing runs of the advanced generation of detectors. Besides all of the events previously announced (GW150914, GW151012, GW151226, GW170104, GW170608, and GW170814) [5–7,10–13], this includes the four new GW events reported in [14] (GW170729, GW170809, GW170818, and GW170823). We do not investigate any of the marginal triggers in GWTC-1, which have a false-alarm rate (FAR) greater than one per year. Table I displays a complete list of

the events we consider. Tests of GR on the binary neutron star event GW170817 are described in [8].

The search results in [14] originate from two modeled searches and one weakly modeled search [5,11,14,15]. The modeled searches use templates based on GR to find candidate events and to assess their significance. However, detection by such searches does not in itself imply full compatibility of the signal with GR [16,17]. The weakly modeled search relies on coherence of signals between multiple detectors, as expected for an astrophysical source. While it assumes that the morphology of the signal resembles a chirp (whose frequency increases with time), as expected for a compact binary coalescence, it does not assume that the detailed waveform shape agrees with GR. A transient signal strongly deviating from GR would likely be found by the weakly modeled search, even if missed by the modeled searches. So far, however, all significant [FAR < (1 yr)⁻¹] transient signals found by the weakly modeled search were also found by at least one of the modeled searches [14].

At present, there are no complete theories of gravity other than GR that are mathematically and physically viable and provide well-defined alternative predictions for the waveforms arising from the coalescence of two black holes (if, indeed, these theories even admit

*Full author list given at the end of the article.

black holes).¹ Thus, we cannot test GR by direct comparison with other specific theories. Instead, we can (i) check the consistency of the GR predictions with the data and (ii) introduce *ad hoc* modifications in GR waveforms to determine the degree to which the values of the deviation parameters agree with GR.

These methods are agnostic to any particular choice of alternative theory. For the most part, our results should therefore be interpreted as observational constraints on possible GW phenomenologies, independent of the overall suitability or well-posedness of any specific alternative to GR. These limits are useful in providing a quantitative indication of the degree to which the data are described by GR; they may also be interpreted more specifically in the context of any given alternative to produce constraints, if applicable.

In particular, with regard to the consistency of the GR predictions (i), we (a) look for residual power after subtracting the best-fitting GR waveform from the data, and (b) evaluate the consistency of the high- and low-frequency components of the observed signal. With regard to deviations from GR (ii), we separately introduce parametrizations for (a) the emitted waveform, and (b) its propagation. The former could be viewed as representing possible GR modifications in the strong-field region close to the binary, while the latter would correspond to weak-field modifications away from the source. Although we consider these independently, modifications to GW propagation would most likely be accompanied by modifications to GW generation in any given extension of GR. We have also checked that none of the events discussed here provide stronger constraints on models with purely vector and purely scalar GW polarizations than those previously published in [7,8]. Our analyses do not reveal any inconsistency of the data with the predictions of GR. These results supersede all our previous testing GR results on the binary black hole signals found in O1 and O2 [4–7]. In particular, the previously published residuals and propagation test results were affected by a slight normalization issue.

Limits on deviations from GR for individual events are dominated by statistical errors due to detector noise. These errors can be reduced by appropriately combining results from multiple events. Sources of systematic errors, on the other hand, include uncertainties in the detector calibration and power spectral density (PSD) estimation and errors in the modeling of waveforms in GR. Detector calibration uncertainties are modeled as corrections to the measured detector response function and are marginalized over. Studies on the

effect of PSD uncertainties are currently ongoing. A full characterization of the systematic errors due to the GR waveform models that we employ is beyond the scope of this study; some investigations can be found in [21–25].

This paper is organized as follows. Section II provides an overview of the data sets employed here, while Sec. III details which GW events are used to produce the individual and combined results presented in this paper. In Sec. IV we explain the gravitational waveforms and data analysis formalisms which our tests of GR are based on, before we present the results in the following sections. Section V contains two signal consistency tests: the residuals test in VA and the inspiral-merger-ringdown consistency test in VB. Results from parametrized tests are given in Sec. VI for GW generation, and in Sec. VII for GW propagation. We briefly discuss the study of GW polarizations in Sec. VIII. Finally, we conclude in Sec. IX. We give results for individual events and some checks on waveform systematics in the Appendix.

The results of each test and associated data products can be found in Ref. [26]. The GW strain data for all the events considered are available at the Gravitational Wave Open Science Center [27].

II. DATA, CALIBRATION, AND CLEANING

The first observing run of Advanced LIGO (O1) lasted from September 12th, 2015 to January 19th, 2016. The second observing run (O2) lasted from November 30th, 2016 to August 25th, 2017, with the Advanced Virgo observatory joining on August 1st, 2017. This paper includes all GW events originating from the coalescence of two black holes found in these two data sets and published in [5,14].

The GW detector’s response to changes in the differential arm length (the interferometer’s degree of freedom most sensitive to GWs) must be calibrated using independent, accurate, absolute references. The LIGO detectors use photon recoil (radiation pressure) from auxiliary laser systems to induce mirror motions that change the arm cavity lengths, allowing a direct measure of the detector response [28–30]. Calibration of Virgo relies on measurements of Michelson interference fringes as the main optics swing freely, using the primary laser wavelength as a fiducial length. Subsequent measurements propagate the calibration to arrive at the final detector response [31,32]. These complex-valued, frequency-dependent measurements of the LIGO and Virgo detectors’ response yield the uncertainty in their respective estimated amplitude and phase of the GW strain output. The amplitude and phase correction factors are modeled as cubic splines and marginalized over in the estimation of astrophysical source parameters [14,33–35]. Additionally, the uncertainty in the time stamping of Virgo data (much larger than the LIGO timing uncertainty, which is included in the phase correction factor) is also accounted for in the analysis.

Postprocessing techniques to subtract noise contributions and frequency lines from the data around gravitational-wave

¹There are very preliminary simulations of scalar waveforms from binary black holes in the effective field theory (EFT) framework in alternative theories [18,19], and the leading corrections to the gravitational waveforms in head-on collisions [20], but these simulations require much more development before their results can be used in gravitational-wave data analysis. There are also concerns about the mathematical viability of the theories considered when they are not treated in the EFT framework.

TABLE I. The GW events considered in this paper, separated by observing run. The first block of columns gives the names of the events and lists some of their relevant properties obtained using GR waveforms (luminosity distance D_L , source frame total mass M_{tot} and final mass M_f , and dimensionless final spin a_f). The next block of columns gives the significance, measured by the FAR, with which each event was detected by each of the three searches employed, as well as the matched filter signal-to-noise ratio from the stochastic sampling analyses with GR waveforms. An ellipsis indicates that an event was not identified by a search. The parameters and SNR values give the medians and 90% credible intervals. All the events except for GW151226 and GW170729 are consistent with a binary of nonspinning black holes (when analyzed assuming GR). See [14] for more details about all the events. The last block of columns indicates which GR tests are performed on a given event: RT = residuals test (Sec. VA); IMR = inspiral-merger-ringdown consistency test (Sec. VB); PI and PPI = parametrized tests of GW generation for inspiral and postinspiral phases (Sec. VI); MDR = modified GW dispersion relation (Sec. VII). The events with bold names are used to obtain the combined results for each test.

| Event | Properties | | | | FAR | | | | GR tests performed | | | | |
|--------------------------------|----------------------------------------|----------------------------------------|----------------------------------------|----------------------------------------|----------------------------|-----------------------------|--------------------------|--------------------------------------|--------------------|-----|-----|-----|-----|
| | D_L [Mpc] | M_{tot} [M_\odot] | M_f [M_\odot] | a_f | PYCBC [yr^{-1}] | GSTLAL [yr^{-1}] | CWB [yr^{-1}] | SNR | RT | IMR | PI | PPI | MDR |
| GW150914 ^a | 440 ⁺¹⁵⁰ ₋₁₇₀ | 66.1 ^{+3.8} _{-3.3} | 63.1 ^{+3.4} _{-3.0} | 0.69 ^{+0.05} _{-0.04} | $< 1.5 \times 10^{-5}$ | $< 1.0 \times 10^{-7}$ | $< 1.6 \times 10^{-4}$ | 25.3 ^{+0.1} _{-0.2} | ✓ | ✓ | ✓ | ✓ | ✓ |
| GW151012 ^a | 1080 ⁺⁵⁵⁰ ₋₄₉₀ | 37.2 ^{+10.6} _{-3.9} | 35.6 ^{+10.8} _{-3.8} | 0.67 ^{+0.13} _{-0.11} | 0.17 | 7.9×10^{-3} | ... | 9.2 ^{+0.3} _{-0.4} | ✓ | ... | ... | ✓ | ✓ |
| GW151226 ^{a,b} | 450 ⁺¹⁸⁰ ₋₁₉₀ | 21.5 ^{+6.2} _{-1.5} | 20.5 ^{+6.4} _{-1.5} | 0.74 ^{+0.07} _{-0.05} | $< 1.7 \times 10^{-5}$ | $< 1.0 \times 10^{-7}$ | 0.02 | 12.4 ^{+0.2} _{-0.3} | ✓ | ... | ✓ | ... | ✓ |
| GW170104 | 990 ⁺⁴⁴⁰ ₋₄₃₀ | 51.0 ^{+5.3} _{-4.1} | 48.9 ^{+5.1} _{-4.0} | 0.66 ^{+0.08} _{-0.11} | $< 1.4 \times 10^{-5}$ | $< 1.0 \times 10^{-7}$ | 2.9×10^{-4} | 14.0 ^{+0.2} _{-0.3} | ✓ | ✓ | ✓ | ✓ | ✓ |
| GW170608 | 320 ⁺¹²⁰ ₋₁₁₀ | 18.6 ^{+3.2} _{-0.7} | 17.8 ^{+3.4} _{-0.7} | 0.69 ^{+0.04} _{-0.04} | $< 3.1 \times 10^{-4}$ | $< 1.0 \times 10^{-7}$ | 1.4×10^{-4} | 15.6 ^{+0.2} _{-0.3} | ✓ | ... | ✓ | ✓ | ✓ |
| GW170729 ^c | 2840 ⁺¹⁴⁰⁰ ₋₁₃₆₀ | 84.4 ^{+15.8} _{-11.1} | 79.5 ^{+14.7} _{-10.2} | 0.81 ^{+0.07} _{-0.13} | 1.4 | 0.18 | 0.02 | 10.8 ^{+0.4} _{-0.5} | ✓ | ✓ | ... | ✓ | ✓ |
| GW170809 | 1030 ⁺³²⁰ ₋₃₉₀ | 59.0 ^{+5.4} _{-4.1} | 56.3 ^{+5.2} _{-3.8} | 0.70 ^{+0.08} _{-0.09} | 1.4×10^{-4} | $< 1.0 \times 10^{-7}$ | ... | 12.7 ^{+0.2} _{-0.3} | ✓ | ✓ | ... | ✓ | ✓ |
| GW170814 | 600 ⁺¹⁵⁰ ₋₂₂₀ | 55.9 ^{+3.4} _{-2.6} | 53.2 ^{+3.2} _{-2.4} | 0.72 ^{+0.07} _{-0.05} | $< 1.2 \times 10^{-5}$ | $< 1.0 \times 10^{-7}$ | $< 2.1 \times 10^{-4}$ | 17.8 ^{+0.3} _{-0.3} | ✓ | ✓ | ✓ | ✓ | ✓ |
| GW170818 | 1060 ⁺⁴²⁰ ₋₃₈₀ | 62.2 ^{+5.2} _{-4.1} | 59.4 ^{+4.9} _{-3.8} | 0.67 ^{+0.07} _{-0.08} | ... | 4.2×10^{-5} | ... | 11.9 ^{+0.3} _{-0.4} | ✓ | ✓ | ... | ✓ | ✓ |
| GW170823 | 1940 ⁺⁹⁷⁰ ₋₉₀₀ | 68.7 ^{+10.8} _{-8.1} | 65.4 ^{+10.1} _{-7.4} | 0.72 ^{+0.09} _{-0.12} | $< 3.3 \times 10^{-5}$ | $< 1.0 \times 10^{-7}$ | 2.1×10^{-3} | 12.0 ^{+0.2} _{-0.3} | ✓ | ✓ | ... | ✓ | ✓ |

^aThe FARs for these events differ from those in [5] because the data were reanalyzed with the new pipeline statistics used in O2 (see [14] for more details).

^bAt least one black hole has dimensionless spin > 0.28 (99% credible level).

^cThis event has a higher significance in the unmodeled search than in the modeled searches. Additionally, at least one black hole has dimensionless spin > 0.27 (99% credible level).

events were developed in O2 and introduced in [7,13,36], for the astrophysical parameter estimation of GW170608, GW170814, and GW170817. This noise subtraction was achieved using optimal Wiener filters to calculate coupling transfer functions from auxiliary sensors [37]. A new, optimized parallelizable method in the frequency domain [38] allows large scale noise subtraction on LIGO data. All of the O2 analyses presented in this manuscript use the noise-subtracted data set with the latest calibration available. The O1 data set is the same used in previous publications, as the effect of noise subtraction is expected to be negligible. Reanalysis of the O1 events is motivated by improvements in the parameter estimation pipeline, an improved frequency-dependent calibration, and the availability of new waveform models.

III. EVENTS AND SIGNIFICANCE

We present results for all confident detections of binary black hole events in GTWC-1 [9], i.e., all such events detected during O1 and O2 with a FAR lower than one per year, as published in [14]. The central columns of Table I list the FARs of each event as evaluated by the three search pipelines used in [14]. Two of these pipelines (PYCBC and

GSTLAL) rely on waveform templates computed from binary black hole coalescences in GR. Making use of a measure of significance that assumes the validity of GR could potentially lead to biases in the selection of events to be tested, systematically disfavoring signals in which a GR violation would be most evident. Therefore, it is important to consider the possibilities that (1) there were GW signals with such large deviations from GR that they were missed entirely by the modeled searches, and (2) there were events that were picked up by the modeled searches but classified as marginal (and thus excluded from our analysis) because of their significant deviations from GR.

These worries can largely be dispelled by considering the third GW search pipeline, the coherent WaveBurst (CWB) weakly modeled search presented in [14]. This CWB search [15,39,40] was tuned to detect chirping signals—like those that would be expected from compact binary coalescences—but was not tuned to any specific GR predictions.² CWB is most sensitive to short signals

²Chirping signals from compact binary coalescences are a feature of many theories of gravity. All that is required is that the orbital frequency increases as the binary radiates energy and angular momentum in GWs.

from high-mass binary black holes. It is still able to detect signals from lower mass binaries (e.g., GW151226), though with reduced significance compared to the modeled searches. Thus, a signal from a low-mass binary, or a marginal event, with a significant departure from the GR predictions (hence not detected by the GR modeled searches) would not necessarily be detected by the CWB search with a FAR $< (1 \text{ yr})^{-1}$. However, if there is a population of such signals, they will not all be weak and/or from low-mass binaries. Thus, one would expect some of the signals in the population to be detected by CWB, even if they evade detection by the modeled searches.

All signals detected by the CWB search with FAR $< (1 \text{ yr})^{-1}$ were also found by at least one modeled search with FAR $< (1 \text{ yr})^{-1}$. Given the above considerations, this is evidence that our analysis does not exclude chirping GW signals that were missed in the modeled searches because of drastic departures from GR. Similarly, this is also evidence against the possibility of marginal events representing a population of GR-deviating signals, as none of them show high significance [FAR $< (1 \text{ yr})^{-1}$] in the CWB search only. Thus, we believe that we have not biased our analysis by considering only the ten events with FAR $< (1 \text{ yr})^{-1}$, as published in [14].

We consider each of the GW events individually, carrying out different analyses on a case-by-case basis. Some of the tests presented here, such as the inspiral-merger-ringdown (IMR) consistency test in Sec. VB and the parametrized tests in Sec. VI, distinguish between the inspiral and the postinspiral regimes of the signal. The separation between these two regimes is performed in the frequency domain, choosing a particular cutoff frequency determined by the parameters of the event. Larger-mass systems merge at lower frequencies, presenting a short inspiral signal in band; lower mass systems have longer observable inspiral signals, but the detector's sensitivity decreases at higher frequencies and hence the postinspiral signal becomes less informative. Therefore, depending on the total mass of the system, a particular signal might not provide enough information within the sensitive frequency band of the GW detectors for all analyses.

As a proxy for the amount of information that can be extracted from each part of the signal, we calculate the signal-to-noise ratio (SNR) of the inspiral and the postinspiral parts of the signals separately. We only apply inspiral (postinspiral) tests if the inspiral (postinspiral) SNR is greater than 6. Each test uses a different inspiral-cutoff frequency, and hence they assign different SNRs to the two regimes (details provided in the relevant section for each test). In Table I we indicate which analyses have been performed on which

event, based on this frequency and the corresponding SNR.³

In addition to the individual analysis of each event, we derive combined constraints on departures from GR using multiple signals simultaneously. Constraints from individual events are largely dominated by statistical uncertainties due to detector noise. Combining events together can reduce such statistical errors on parameters that take consistent values across all events. However, it is impossible to make joint probabilistic statements from multiple events without prior assumptions about the nature of each observation and how it relates to others in the set. This means that, although there are well-defined statistical procedures for producing joint results, there is no unique way of doing so.

In light of this, we adopt what we take to be the most straightforward strategy, although future studies may follow different criteria. First, in combining events we assume that deviations from GR are manifested equally across events, independent of source properties. This is justified for studies of modified GW propagation, since those effects should not depend on the source.⁴ For other analyses, it is quite a strong assumption to take all deviations from GR to be independent of source properties. Such combined tests should not be expected to necessarily reveal generic source-dependent deviations, although they might if the departures from GR are large enough (see, e.g., [41]). Future work may circumvent this issue by combining marginalized likelihood ratios (Bayes factors), instead of posterior probability distributions [42]. More general ways of combining results are discussed and implemented in Refs. [43,44].

Second, we choose to produce combined constraints only from events that were found in both modeled searches (PYCBC [45–47] and GSTLAL [48,49]) with a FAR of at most one per one thousand years. This ensures that there is a very small probability of inclusion of a nonastrophysical event. The events used for the combined results are indicated with bold names in Table I. The events thus excluded from the combined analysis have low SNR and would therefore contribute only marginally to tightened constraints. Excluding marginal events from our analyses amounts to assigning a null *a priori* probability to the possibility that those data contain any information about the tests in question. This is, in a sense, the most conservative choice.

In summary, we enforce two significance thresholds: FAR $< (1 \text{ yr})^{-1}$, for single-event analyses, and FAR $< (1000 \text{ yr})^{-1}$, for combined results. This two-tiered setup

³While we perform these tests on all events with SNR > 6 in the appropriate regime, in a few cases the results appear uninformative and the posterior distribution extends across the entire prior considered. Since the results are prior dependent, upper limits should not be set from these individual analyses. See Sec. A 3 of the Appendix for details.

⁴Propagation effects do depend critically on source distance. However, this dependence is factored out explicitly, in a way that allows for combining events as we do here (see Sec. VII).

allows us to produce conservative joint results by including only the most significant events, while also providing information about a broader (less significant) set of triggers. This is intended to enable the interested reader to combine individual results with less stringent criteria and under different statistical assumptions, according to their specific needs and tolerance for false positives. In the future, we may adapt our thresholds depending on the rate of detections.

IV. PARAMETER INFERENCE

The starting point for all the analyses presented here are waveform models that describe the GWs emitted by coalescing black hole binaries. The GW signature depends on the intrinsic parameters describing the binary as well as the extrinsic parameters specifying the location and orientation of the source with respect to the detector network. The intrinsic parameters for circularized black-hole binaries in GR are the two masses m_i of the black holes and the two spin vectors \vec{S}_i defining the rotation of each black hole, where $i \in \{1, 2\}$ labels the two black holes. We assume that the binary has negligible orbital eccentricity, as is expected to be the case when the binary enters the band of ground-based detectors [50,51] (except in some more extreme formation scenarios,⁵ e.g., [60–63]). The extrinsic parameters comprise four parameters that specify the space-time location of the binary black hole, namely, the sky location (right ascension and declination), the luminosity distance, and the time of coalescence. In addition, there are three extrinsic parameters that determine the orientation of the binary with respect to Earth, namely, the inclination angle of the orbit with respect to the observer, the polarization angle, and the orbital phase at coalescence.

We employ two waveform families that model binary black holes in GR: the effective-one-body based SEOBNRv4 [21] waveform family that assumes nonprecessing spins for the black holes (we use the frequency domain reduced order model SEOBNRv4_ROM for reasons of computational efficiency), and the phenomenological waveform family IMRPHENOMPv2 [22,64,65] that models the effects of precessing spins using two effective parameters by twisting up the underlying aligned-spin model. We use IMRPHENOMPv2 to obtain all the main results given in this paper, and use SEOBNRv4 to check the robustness of these results, whenever possible. When we use IMRPHENOMPv2, we impose a prior $m_1/m_2 \leq 18$ on the mass ratio, as the waveform family is not calibrated against numerical-relativity (NR) simulations for $m_1/m_2 > 18$. We do not impose a similar prior when using SEOBNRv4, since it includes information about the extreme mass ratio limit. Neither of these waveform models

includes the full spin dynamics (which requires six spin parameters). Fully precessing waveform models have been recently developed [24,66–69] and will be used in future applications of these tests.

The waveform models used in this paper do not include the effects of subdominant (nonquadrupole) modes, which are expected to be small for comparable-mass binaries [70,71]. The first generation of binary black hole waveform models including spin and higher order modes has recently been developed [68,69,72–74]. Preliminary results in [14], using NR simulations supplemented by NR surrogate waveforms, indicate that the higher mode content of the GW signals detected by Advanced LIGO and Virgo is weak enough that models without the effect of subdominant modes do not introduce substantial biases in the intrinsic parameters of the binary. For unequal-mass binaries, the effect of the non-quadrupole modes is more pronounced [75], particularly when the binary’s orientation is close to edge on. In these cases, the presence of nonquadrupole modes can show up as a deviation from GR when using waveforms that only include the quadrupole modes, as was shown in [76]. Applications of tests of GR with the new waveform models that include nonquadrupole modes will be carried out in the future.

We believe that our simplifying assumptions on the waveform models (zero eccentricity, simplified treatment of spins, and neglect of subdominant modes) are justified by astrophysical considerations and previous studies. Indeed, as we show in the remainder of the paper, the observed signals are consistent with the waveform models. Of course, had our analyses resulted in evidence for violations of GR, we would have had to revisit these simplifications very carefully.

The tests described in this paper are performed within the framework of Bayesian inference, by means of the LALINFERENCE code [34] in the LIGO Scientific Collaboration Algorithm Library Suite (LALSuite) [77]. We estimate the PSD using the BAYESWAVE code [78,79], as described in Appendix B of [14]. Except for the residuals test described in Sec. VA, we use the waveform models described in this section to estimate from the data the posterior distributions of the parameters of the binary. These include not only the intrinsic and extrinsic parameters mentioned above, but also other parameters that describe possible departures from the GR predictions. Specifically, for the parametrized tests in Secs. VI and VII, we modify the phase $\Phi(f)$ of the frequency-domain waveform

$$\tilde{h}(f) = A(f)e^{i\Phi(f)}. \quad (1)$$

For the GR parameters, we use the same prior distributions as the main parameter estimation analysis described in [14], though for a number of the tests we need to extend the ranges of these priors to account for correlations with the non-GR parameters, or for the fact that only a portion of the signal is analyzed (as in Sec. VB). We also use the same

⁵These scenarios could occur often enough, compared to the expected rate of detections, that the inclusion of eccentricity in waveform models is a necessity for tests of GR in future observing runs; see, e.g., [52–59] for recent work on developing such waveform models.

low-frequency cutoffs for the likelihood integral as in [14], i.e., 20 Hz for all events except for GW170608, where 30 Hz is used for LIGO Hanford, as discussed in [13], and GW170818, where 16 Hz is used for all three detectors. For the model agnostic residual test described in Sec. VA, we use the BAYESWAVE code [78] which describes the GW signals in terms of a number of Morlet-Gabor wavelets.

V. CONSISTENCY TESTS

A. Residuals test

One way to evaluate the ability of GR to describe GW signals is to subtract the best-fit template from the data and make sure the residuals have the statistical properties expected of instrumental noise. This largely model-independent test is sensitive to a wide range of possible disagreements between the data and our waveform models, including those caused by deviations from GR and by modeling systematics. This analysis can look for GR violations without relying on specific parametrizations of the deviations, making it a versatile tool. Results from a similar study on our first detection were already presented in [4].

In order to establish whether the residuals agree with noise (Gaussian or otherwise), we proceed as follows. For each event in our set, we use LALINFERENCE and the IMRPHENOMPv2 waveform family to obtain an estimate of the best-fit (i.e., maximum likelihood) binary black hole waveform based on GR. This waveform incorporates factors that account for uncertainty in the detector calibration, as described in Sec. II. This best-fit waveform is then subtracted from the data to obtain residuals for a 1 second window centered on the trigger time reported in [14].⁶ If the GR-based model provides a good description of the signal, we expect the resulting residuals at each detector to lack any significant coherent SNR beyond what is expected from noise fluctuations. We compute the coherent SNR using BAYESWAVE, which models the multidetector residuals as a superposition of incoherent Gaussian noise and an elliptically polarized coherent signal. The residual network SNR reported by BAYESWAVE is the SNR that would correspond to such a coherent signal.

In particular, for each event, BAYESWAVE produces a distribution of possible residual signals consistent with the data, together with corresponding *a posteriori* probabilities. This is trivially translated into a probability distribution over the coherent residual SNR. We summarize each of these distributions by computing the corresponding 90% credible upper limit (SNR_{90}). This produces one number per event that represents an upper bound on the coherent power that could be present in its residuals.

We may translate the SNR_{90} into a measure of how well the best-fit templates describe the signals in our data. We do this through the fitting factor [80], $\text{FF} := \text{SNR}_{\text{GR}} / (\text{SNR}_{\text{res}}^2 + \text{SNR}_{\text{GR}}^2)^{1/2}$, where SNR_{res} is the coherent residual SNR and SNR_{GR} is the network SNR of the best-fit template (see Table I for network SNRs). By setting $\text{SNR}_{\text{res}} = \text{SNR}_{90}$, we produce a 90% credible lower limit on the fitting factor (FF_{90}). Because the FF is itself a lower limit on the overlap between the true and best-fit templates, so is FF_{90} . As in [4], we may then assert that the disagreement between the true waveform and our GR-based template is at most $(1 - \text{FF}_{90}) \times 100\%$. This is interesting as a measure of the sensitivity of our test, but does not tell us about the consistency of the residuals with instrumental noise.

To assess whether the obtained residual SNR_{90} values are consistent with detector noise, we run an identical BAYESWAVE analysis on 200 different sets of noise-only detector data near each event. This allows us to estimate the p -value for the null hypothesis that the residuals are consistent with noise. The p -value gives the probability of noise producing coherent power with SNR_{90}^n greater than or equal to the residual value SNR_{90} , i.e., $p := P(\text{SNR}_{90}^n \geq \text{SNR}_{90} | \text{noise})$. In that sense, a smaller p -value indicates a smaller chance that the residual power arose from instrumental noise only. For each event, our estimate of p is produced from the fraction of noise instantiations that yielded $\text{SNR}_{90}^n \geq \text{SNR}_{90}$ (that is, from the empirical survival function).⁷

Our results are summarized in Table II. For each event, we present the values of the residual SNR_{90} , the lower limit on the fitting factor (FF_{90}), and the SNR_{90} p -value. The background distributions that resulted in those p -values are shown in Fig. 1. In Fig. 1 we represent these distributions through the empirical estimate of their survival functions, i.e., $p(\text{SNR}_{90}) = 1 - \text{CDF}(\text{SNR}_{90})$, with CDF being the cumulative distribution function. Figure 1 also displays the actual value of SNR_{90} measured from the residuals of each event (dotted vertical line). In each case, the height of the curve evaluated at the SNR_{90} measured for the corresponding detection yields the p -value reported in Table II (markers in Fig. 1).

The values of residual SNR_{90} vary widely among events because they depend on the specific state of the instruments at the time of detection: segments of data with elevated noise levels are more likely to result in spurious coherent residual power, even if the signal agrees with GR. In particular, the background distributions for events seen by three detectors are qualitatively different from those seen by only two. This is both due to (i) the fact that BAYESWAVE is configured to expect the SNR to increase with the number of detectors and (ii) the fact that Virgo data present

⁶The analysis is sensitive only to residual power in that 1 s window due to technicalities related to how BAYESWAVE handles its sine-Gaussian basis elements [78,79].

⁷Computing p -values would not be necessary if the noise was perfectly Gaussian, in which case we could predict the noise-only distribution of SNR_{90}^n from first principles.

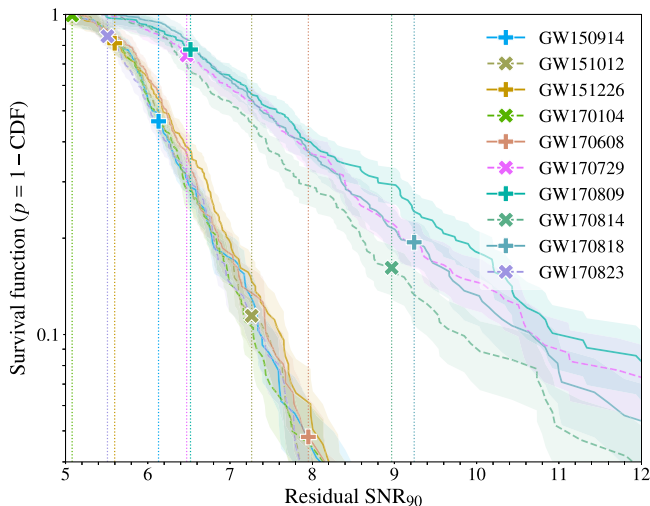


FIG. 1. Survival function ($p = 1 - \text{CDF}$) of the 90% credible upper limit on the network SNR (SNR_{90}) for each event (solid or dashed curves), compared to the measured residual values (vertical dotted lines). For each event, the value of the survival function at the measured SNR_{90} gives the p -value reported in Table II (markers). The colored bands correspond to uncertainty regions for a Poisson process and have half width $\pm p/\sqrt{N}$, with N being the number of noise-only instantiations that yielded SNR_{90}^0 greater than the abscissa value.

a higher rate of non-Gaussianities than LIGO. We have confirmed that both these factors play a role by studying the background SNR_{90} distributions for real data from each possible pair of detectors, as well as distributions over simulated Gaussian noise. Specifically, removing Virgo from the analysis results in a reduction in the coherent residual power for GW170729 ($\text{SNR}_{90}^{\text{HL}} = 6.5$), GW170809 ($\text{SNR}_{90}^{\text{HL}} = 6.3$), GW170814 ($\text{SNR}_{90}^{\text{HL}} = 6.0$), and GW170818 ($\text{SNR}_{90}^{\text{HL}} = 7.2$).

The event-by-event variation of SNR_{90} is also reflected in the values of FF_{90} . GW150914 provides the strongest result with $\text{FF}_{90} = 0.97$, which corresponds to an upper limit of 3% on the magnitude of potential deviations from our GR-based template,⁸ in the specific sense defined in [4] and discussed above. On the other hand, GW170818 yields the weakest result with $\text{FF}_{90} = 0.78$ and a corresponding upper limit on waveform disagreement of $1 - \text{FF}_{90} = 22\%$. The average FF_{90} over all events is 0.88.

The set of p -values shown in Table II is consistent with all coherent residual power being due to instrumental noise. Assuming that this is indeed the case, we expect the p -values to be uniformly distributed over $[0, 1]$, which explains the variation in Table II. With only ten events,

⁸This value is better than the one quoted in [4] by 1 percentage point. The small difference is explained by several factors, including that paper’s use of the maximum *a posteriori* waveform (instead of maximum likelihood) and 95% (instead of 90%) credible intervals, as well as improvements in data calibration.

TABLE II. Results of the residuals analysis. For each event, this table presents the 90% credible upper limit on the reconstructed network SNR after subtraction of the best-fit GR waveform (SNR_{90}), a corresponding lower limit on the fitting factor (FF_{90} in the text), and the SNR_{90} p -value. SNR_{90} is a measure of the maximum possible coherent signal power not captured by the best-fit GR template, while the p -value is an estimate of the probability that instrumental noise produced such SNR_{90} or higher. We also indicate which interferometers (IFOs) were used in the analysis of a given event, either the two Advanced LIGO detectors (HL) or the two Advanced LIGO detectors plus Advanced Virgo (HLV). See Sec. VA in the main text for details.

| Event | IFOs | Residual SNR_{90} | Fitting factor | p -value |
|----------|------|----------------------------|----------------|------------|
| GW150914 | HL | 6.1 | ≥ 0.97 | 0.46 |
| GW151012 | HL | 7.3 | ≥ 0.79 | 0.11 |
| GW151226 | HL | 5.6 | ≥ 0.91 | 0.81 |
| GW170104 | HL | 5.1 | ≥ 0.94 | 0.99 |
| GW170608 | HL | 7.9 | ≥ 0.89 | 0.05 |
| GW170729 | HLV | 6.5 | ≥ 0.85 | 0.74 |
| GW170809 | HLV | 6.5 | ≥ 0.88 | 0.78 |
| GW170814 | HLV | 8.9 | ≥ 0.88 | 0.16 |
| GW170818 | HLV | 9.2 | ≥ 0.78 | 0.19 |
| GW170823 | HL | 5.5 | ≥ 0.90 | 0.86 |

however, it is difficult to obtain strong quantitative evidence of the uniformity of this distribution. Nevertheless, we follow Fisher’s method [81] to compute a meta p -value for the null hypothesis that the individual p -values in Table II are uniformly distributed. We obtain a meta p -value of 0.4, implying that there is no evidence for coherent residual power that cannot be explained by noise alone. All in all, this means that there is no statistically significant evidence for deviations from GR.

B. Inspiral-merger-ringdown consistency test

The inspiral-merger-ringdown consistency test for binary black holes [41,82] checks the consistency of the low-frequency part of the observed signal (roughly corresponding to the inspiral of the black holes) with the high-frequency part (to a good approximation, produced by the postinspiral stages).⁹ The cutoff frequency f_c between the two regimes is chosen as the frequency of the innermost stable circular orbit of a Kerr black hole [83], with mass and dimensionless spin computed by applying NR fits [84–87] to the median values of the posterior distributions of the initial masses and spherical coordinate components of the spins. This determination of f_c is performed separately for each event and based on parameter inference of the full

⁹Note that this is not exactly equal to testing the consistency between the early and late part of the waveform in time domain, because the low-frequency part of the signal could be “contaminated” by power from late times and vice versa. In practice, this effect is negligible with our choice of cutoff frequencies. See [41] for a discussion.

TABLE III. Results from the inspiral-merger-ringdown consistency test for selected binary black hole events. f_c denotes the cutoff frequency used to demarcate the division between the inspiral and postinspiral regimes; ρ_{IMR} , ρ_{insp} , and ρ_{postinsp} are the median values of the SNR in the full signal, the inspiral part, and the postinspiral part, respectively; and the GR quantile denotes the fraction of the posterior enclosed by the isoproability contour that passes through the GR value, with smaller values indicating better consistency with GR. (Note, however, that the posterior distribution is broader for smaller SNRs, and hence the GR quantile is typically smaller in such cases. This effect is further complicated by the randomness of the noise.)

| Event | f_c [Hz] | ρ_{IMR} | ρ_{insp} | ρ_{postinsp} | GR quantile [%] |
|----------|------------|---------------------|----------------------|--------------------------|-----------------|
| GW150914 | 132 | 25.3 | 19.4 | 16.1 | 55.5 |
| GW170104 | 143 | 13.7 | 10.9 | 8.5 | 24.4 |
| GW170729 | 91 | 10.7 | 8.6 | 6.9 | 10.4 |
| GW170809 | 136 | 12.7 | 10.6 | 7.1 | 14.7 |
| GW170814 | 161 | 16.8 | 15.3 | 7.2 | 7.8 |
| GW170818 | 128 | 12.0 | 9.3 | 7.2 | 25.5 |
| GW170823 | 102 | 11.9 | 7.9 | 8.5 | 80.4 |

signal (see Table III for values of f_c).¹⁰ The binary's parameters are then estimated independently from the low- (high-) frequency parts of the data by restricting the noise-weighted integral in the likelihood calculation to frequencies below (above) this frequency cutoff f_c . For each of these independent estimates of the source parameters, we make use of fits to numerical-relativity simulations given in [84–86] to infer the mass M_f and dimensionless spin magnitude $a_f = c|\vec{S}_f|/(GM_f^2)$ of the remnant black hole.¹¹ If the data are consistent with GR, these two independent estimates have to be consistent with each other [41,82]. Because this consistency test ultimately compares between the inspiral and the postinspiral results, posteriors of both parts must be informative. In the case of low-mass binaries, the SNR in the part $f > f_c$ is insufficient to perform this test, so that we only analyze seven events as indicated in Tables I and III.

In order to quantify the consistency of the two different estimates of the final black hole's mass and spin we define two dimensionless quantities that quantify the fractional difference between them: $\Delta M_f/\bar{M}_f := 2(M_f^{\text{insp}} - M_f^{\text{postinsp}})/(M_f^{\text{insp}} + M_f^{\text{postinsp}})$ and $\Delta a_f/\bar{a}_f := 2(a_f^{\text{insp}} - a_f^{\text{postinsp}})/(a_f^{\text{insp}} + a_f^{\text{postinsp}})$, where the superscripts indicate the

¹⁰The frequency f_c was determined using preliminary parameter inference results, so the values in Table III are slightly different than those that would be obtained using the posterior samples in GWTC-1 [9]. However, the test is robust against small changes in the cutoff frequency [41].

¹¹As in [6], we average the M_f, a_f posteriors obtained by different fits [84–86] after augmenting the fitting formulas for aligned-spin binaries by adding the contribution from in-plane spins [87]. However, unlike in [6,87], we do not evolve the spins before applying the fits, due to technical reasons.

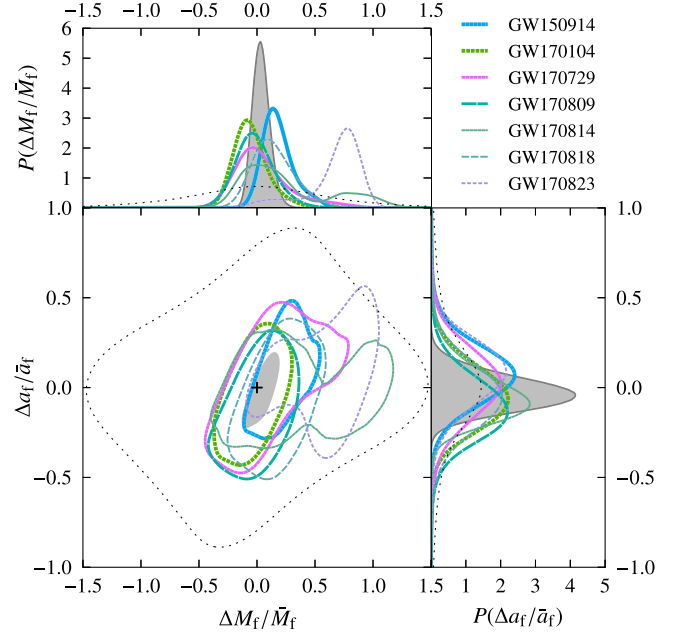


FIG. 2. Results of the inspiral-merger-ringdown consistency test for the selected binary black hole events (see Table I). The main panel shows 90% credible regions of the posterior distributions of $(\Delta M_f/\bar{M}_f, \Delta a_f/\bar{a}_f)$, with the cross marking the expected value for GR. The side panels show the marginalized posteriors for $\Delta M_f/\bar{M}_f$ and $\Delta a_f/\bar{a}_f$. The thin black dashed curve represents the prior distribution, and the grey shaded areas correspond to the combined posteriors from the five most significant events (as outlined in Sec. III and Table I).

estimates of the mass and spin from the inspiral and postinspiral parts of the signal.¹² The posteriors of these dimensionless parameters, estimated from different events, are shown in Fig. 2. For all events, the posteriors are consistent with the GR value ($\Delta M_f/\bar{M}_f = 0, \Delta a_f/\bar{a}_f = 0$). The fraction of the posterior enclosed by the isoproability contour that passes through the GR value (i.e., the GR quantile) for each event is shown in Table III. Figure 2 also shows the posteriors obtained by combining all the events that pass the stronger significance threshold $\text{FAR} < (1000 \text{ yr})^{-1}$, as outlined in Sec. III (see the same section for a discussion of caveats).

The parameter estimation is performed employing uniform priors in component masses and spin magnitudes and isotropic priors in spin directions [14]. This introduces a nonflat prior in the deviation parameters $\Delta M_f/\bar{M}_f$ and $\Delta a_f/\bar{a}_f$, which is shown as a thin, dashed contour in Fig. 2. Posteriors are estimated employing the precessing spin

¹²For black hole binaries with comparable masses and moderate spins, as we consider here, the remnant black hole is expected to have $a_f \gtrsim 0.5$; see, e.g., [84–86] for fitting formulas derived from numerical simulations, or Table I for values of the remnant's spins obtained from GW events. Hence, $\Delta a_f/\bar{a}_f$ is expected to yield finite values.

phenomenological waveform family IMRPHENOMPv2. To assess the systematic errors due to imperfect waveform modeling, we also estimate the posteriors using the effective-one-body based waveform family SEOBNRv4 that models binary black holes with nonprecessing spins. There is no qualitative difference between the results derived using the two different waveform families (see Sec. A 2 of the Appendix).

We see additional peaks in the posteriors estimated from GW170814 and GW170823. Detailed follow-up investigations did not show any evidence of the presence of a coherent signal in multiple detectors that differs from the GR prediction. The second peak in GW170814 is introduced by the posterior of M_f^{postinsp} , while the extra peak in GW170823 is introduced by the posterior of M_f^{insp} . Injection studies in real data around the time of these events, using simulated GR waveforms with parameters consistent with GW170814 and GW170823, suggest that such secondary peaks occur for $\sim 10\%$ of injections. Features in the posteriors of GW170814 and GW170823 are thus consistent with expected noise fluctuations.

VI. PARAMETRIZED TESTS OF GRAVITATIONAL-WAVE GENERATION

A deviation from GR could manifest itself as a modification of the dynamics of two orbiting compact objects, and in particular, the evolution of the orbital (and hence, GW) phase. In an analytical waveform model like IMRPHENOMPv2, the details of the GW phase evolution are controlled by coefficients that are either analytically calculated or determined by fits to NR simulations, always under the assumption that GR is the underlying theory. In this section we investigate deviations from the GR binary dynamics by introducing shifts in each of the individual GW phase coefficients of IMRPHENOMPv2. Such shifts correspond to deviations in the waveforms from the predictions of GR. We then treat these shifts as additional unconstrained GR-violating parameters, which we measure in addition to the standard parameters describing the binary.

The early inspiral of compact binaries is well modeled by the post-Newtonian (PN) approximation [88–91] to GR, which is based on the expansion of the orbital quantities in terms of a small velocity parameter v/c . For a given set of intrinsic parameters, coefficients for the different orders in v/c in the PN series are uniquely determined. A consistency test of GR using measurements of the inspiral PN phase coefficients was first proposed in [92–94], while a generalized parametrization was motivated in [95]. Bayesian implementations based on such parametrized methods were presented and tested in [42,96–98] and were also extended to the postinspiral part of the gravitational-wave signal [99,100]. These ideas were applied to the first GW observation, GW150914 [10], yielding the first bounds on higher-order PN coefficients [4]. Since then, the

constraints have been revised with the binary black hole events that followed, GW151226 in O1 [5] and GW170104 in O2 [6]. More recently, the first such constraints from a binary neutron star merger were placed with the detection of GW170817 [8]. Bounds on parametrized violations of GR from GW detections have been mapped, to leading order, to constraints on specific alternative theories of gravity (see, e.g., [101]). In this paper, we present individual constraints on parametrized deviations from GR for each of the GW sources in O1 and O2 listed in Table I, as well as the tightest combined constraints obtained to date by combining information from all the significant binary black holes events observed so far, as described in Sec. III.

The frequency-domain GW phase evolution $\Phi(f)$ in the early-inspiral stage of IMRPHENOMPv2 is described by a PN expansion, augmented with higher-order phenomenological coefficients. The PN phase evolution is analytically expressed in closed form by employing the stationary phase approximation. The late-inspiral and postinspiral (intermediate and merger-ringdown) stages are described by phenomenological analytical expressions. The transition frequency¹³ from inspiral to intermediate regime is given by the condition $GMf/c^3 = 0.018$, with M being the total mass of the binary in the detector frame, since this is the lowest frequency above which this model was calibrated with NR data [22]. Let us use p_i to collectively denote all of the inspiral and postinspiral parameters $\varphi_i, \alpha_i, \beta_i$, that will be introduced below. Deviations from GR in all stages are expressed by means of relative shifts $\delta\hat{p}_i$ in the corresponding waveform coefficients: $p_i \rightarrow (1 + \delta\hat{p}_i)p_i$, which are used as additional free parameters in our extended waveform models.

We denote the testing parameters corresponding to PN phase coefficients by $\delta\hat{p}_i$, where i indicates the power of v/c beyond leading (Newtonian or 0 PN) order in $\Phi(f)$. The frequency dependence of the corresponding phase term is $f^{(i-5)/3}$. In the parametrized model, i varies from 0 to 7, including the terms with logarithmic dependence at 2.5 and 3 PN. The nonlogarithmic term at 2.5 PN (i.e., $i = 5$) cannot be constrained, because of its degeneracy with a constant reference phase (e.g., the phase at coalescence). These coefficients were introduced in their current form in Eq. (19) of [96]. In addition, we also test for $i = -2$, representing an effective -1 PN term, which is motivated below. The full set of inspiral parameters is thus

$$\{\delta\hat{p}_{-2}, \delta\hat{p}_0, \delta\hat{p}_1, \delta\hat{p}_2, \delta\hat{p}_3, \delta\hat{p}_4, \delta\hat{p}_{5l}, \delta\hat{p}_6, \delta\hat{p}_{6l}, \delta\hat{p}_7\}.$$

Since the -1 PN term and 0.5 PN term are absent in the GR phasing, we parametrize $\delta\hat{p}_{-2}$ and $\delta\hat{p}_1$ as *absolute* deviations, with a prefactor equal to the 0 PN coefficient.

¹³This frequency is different than the cutoff frequency used in the inspiral-merger-ringdown consistency test, as was briefly mentioned in Sec. III.

The -1 PN term of $\delta\hat{\varphi}_2$ can be interpreted as arising from the emission of dipolar radiation. For binary black holes, this could occur in, e.g., alternative theories of gravity where an additional scalar charge is sourced by terms related to curvature [102,103]. At leading order, this introduces a deviation in the -1 PN coefficient of the waveform [104,105]. This effectively introduces a term in the inspiral GW phase, varying with frequency as $f^{-7/3}$, while the gravitational flux is modified as $\mathcal{F}_{\text{GR}} \rightarrow \mathcal{F}_{\text{GR}}(1 + Bc^2/v^2)$. The first bound on $\delta\hat{\varphi}_{-2}$ was published in [8]. The higher-order terms in the above expansion also lead to a modification in the higher-order PN coefficients. Unlike the case of GW170817 (which we study separately in [8]), where the higher-order terms in the expansion of the flux are negligible, the contribution of higher-order terms can be significant in the binary black hole signals that we study here. This prohibits an exact interpretation of the -1 PN term as the strength of dipolar radiation. Hence, this analysis only serves as a test of the presence of an effective -1 PN term in the inspiral phasing, which is absent in GR.

To measure the above GR violations in the post-Newtonian inspiral, we employ two waveform models: (i) the analytical frequency-domain model IMRPHEMOPv2 which also provided the natural parametrization for our tests and (ii) SEOBNRv4, which we use in the form of SEOBNRv4_ROM, a frequency-domain, reduced-order model of the SEOBNRv4 model. The inspiral part of SEOBNRv4 is based on a numerical evolution of the aligned-spin effective-one-body dynamics of the binary and its postinspiral model is phenomenological. The entire SEOBNRv4 model is calibrated against NR simulations. Despite its nonanalytical nature, SEOBNRv4_ROM can also be used to test the parametrized modifications of the early inspiral defined above. Using the method presented in [8], we add deviations to the waveform phase corresponding to a given $\delta\hat{\varphi}_i$ at low frequencies and then taper the corrections to 0 at a frequency consistent with the transition frequency between early-inspiral and intermediate phases used by IMRPHEMOPv2. The same procedure cannot be applied to the later stages of the waveform; thus the analysis performed with SEOBNRv4 is restricted to the post-Newtonian inspiral, cf. Fig. 3.

The analytical descriptions of the intermediate and merger-ringdown stages in the IMRPHEMOPv2 model allow for a straightforward way of parametrizing deviations from GR, denoted by $\{\delta\hat{\beta}_2, \delta\hat{\beta}_3\}$ and $\{\delta\hat{\alpha}_2, \delta\hat{\alpha}_3, \delta\hat{\alpha}_4\}$, respectively, following [100]. Here the parameters $\delta\hat{\beta}_i$ correspond to deviations from the NR-calibrated phenomenological coefficients β_i of the intermediate stage, while the parameters $\delta\hat{\alpha}_i$ refer to modifications of the merger-ringdown coefficients α_i obtained from a combination of phenomenological fits and analytical black hole perturbation theory calculations [22].

Using LALINFERENCE, we calculate posterior distributions of the parameters characterizing the waveform (including those that describe the binary in GR). Our parametrization recovers GR at $\delta\hat{\rho}_i = 0$, so consistency with GR is verified if the posteriors of $\delta\hat{\rho}_i$ have support at 0. We perform the analyses by varying one $\delta\hat{\rho}_i$ at a time; as shown in Ref. [106]; this is fully robust to detecting deviations present in multiple PN-orders. In addition, allowing for a larger parameter space by varying multiple coefficients simultaneously would not improve our efficiency in identifying violations of GR, as it would yield less informative posteriors. A specific alternative theory of gravity would likely yield correlated deviations in many parameters, including modifications that we have not considered here. This would be the target of an exact comparison of an alternative theory with GR, which would only be possible if a complete, accurate description of the inspiral-merger-ringdown signal in that theory was available.

We use priors uniform on $\delta\hat{\rho}_i$ and symmetric around 0. Figure 3 shows the combined posteriors of $\delta\hat{\rho}_i$ (marginalized over all other parameters) estimated from the combination of all the events that cross the significance threshold of $\text{FAR} < (1000 \text{ yr})^{-1}$ in both modeled searches; see Table I. Events with $\text{SNR} < 6$ in the inspiral regime (parameters $\delta\hat{\varphi}_i$) or in the postinspiral regime ($\delta\hat{\beta}_i$ and $\delta\hat{\alpha}_i$ for the intermediate and merger-ringdown parameters, respectively) are not included in the results, since the data from those instances failed to provide useful constraints (see Sec. III for more details). This SNR threshold, however, is not equally effective in ensuring informative

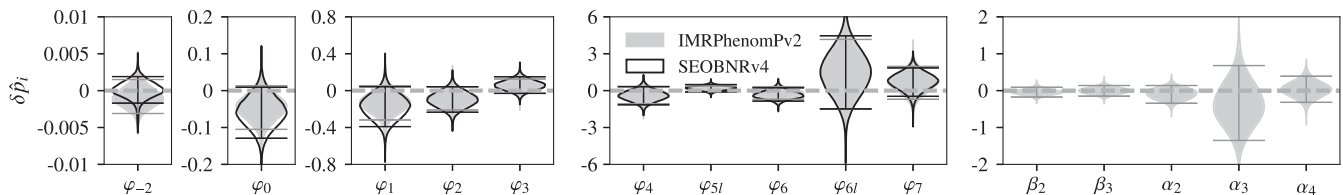


FIG. 3. Combined posteriors for parametrized violations of GR, obtained from all events in Table I with a significance of $\text{FAR} < (1000 \text{ yr})^{-1}$ in both modeled searches. The horizontal lines indicate the 90% credible intervals, and the dashed horizontal line at 0 corresponds to the expected GR values. The combined posteriors on φ_i in the inspiral regime are obtained from the events which in addition exceed the SNR threshold in the inspiral regime (GW150914, GW151226, GW170104, GW170608, and GW170814), analyzed with IMRPHEMOPv2 (grey shaded region) and SEOBNRv4 (black outline). The combined posteriors on the intermediate and merger-ringdown parameters β_i and α_i are obtained from events which exceed the SNR threshold in the postinspiral regime (GW150914, GW170104, GW170608, GW170809, GW170814, and GW170823), analyzed with IMRPHEMOPv2.

results for all cases; see Sec. A 3 in the Appendix for a detailed discussion. In all cases considered, the posteriors are consistent with $\delta\hat{p}_i = 0$ within statistical fluctuations. Bounds on the inspiral coefficients obtained with the two different waveform models are found to be in good agreement with each other. Finally, we note that the event-combining analyses on $\delta\hat{p}_i$ assume that these parametrized violations are constant across all events considered. This assumption should not be made when testing a specific theory that predicts violations that depend on the binary's parameters. Posterior distributions of $\delta\hat{p}_i$ for the individual-event analysis, also showing full consistency with GR, are provided in Sec. A 3 of the Appendix.

Figure 4 shows the 90% upper bounds on $|\delta\hat{\phi}_i|$ for all the individual events which cross the SNR threshold ($\text{SNR} > 6$) in the inspiral regime (the most massive of which is GW150914). The bounds from the combined posteriors are also shown; these include the events which exceed both the SNR threshold in the inspiral regime as well as the significance threshold, namely, GW150914, GW151226, GW170104, GW170608, and GW170814. The bound from the likely lightest mass binary black hole event GW170608 at 1.5 PN is currently the strongest constraint obtained on a positive PN coefficient from a single binary black hole event, as shown in Fig. 4. However, the constraint at this

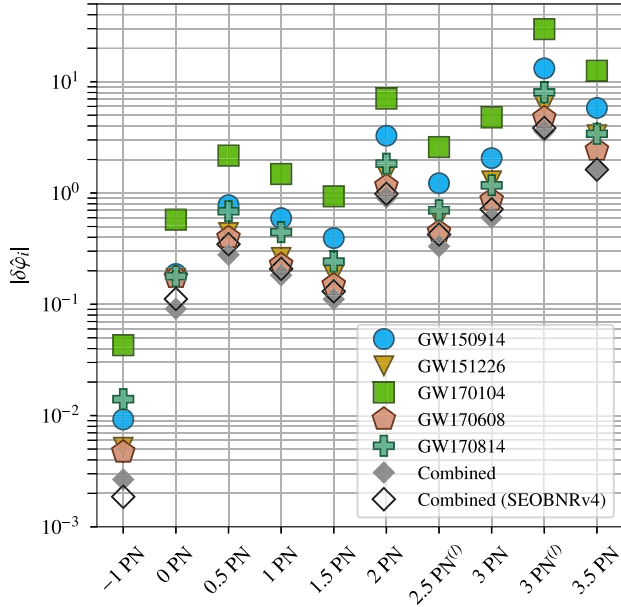


FIG. 4. 90% upper bounds on the absolute magnitude of the GR-violating parameters $\delta\hat{\phi}_n$, from -1 through 3.5 PN in the inspiral phase. At each PN order, we show results obtained from each of the events listed in Table I that cross the SNR threshold in the inspiral regime, analyzed with IMRPHENOMPv2. Bounds obtained from combining posteriors of events detected with a significance that exceeds a threshold of $\text{FAR} < (1000 \text{ yr})^{-1}$ in both modeled searches are shown for both analyses, using IMRPHENOMPv2 (filled diamonds) and SEOBNRv4 (empty diamonds).

order is about five times worse than that obtained from the binary neutron star event GW170817 alone [8]. The -1 PN bound is 2 orders of magnitude better for GW170817 than the best bound obtained here (from GW170608). The corresponding best -1 PN bound coming from the double pulsar PSR J0737–3039 is a few orders of magnitude tighter still, at $|\delta\hat{\phi}_{-2}| \lesssim 10^{-7}$ [104,107]. At 0 PN we find that the bound from GW170608 beats the one from GW170817, but remains weaker than the one from the double pulsar by 1 order of magnitude [107,108]. For all other PN orders, GW170608 also provides the best bounds, which at high PN orders are of the same order of magnitude as the ones from GW170817. Our results can be compared statistically to those obtained by performing the same tests on simulated GR and non-GR waveforms given in [100]. The results presented here are consistent with those of GR waveforms injected into realistic detector data. The combined bounds are the tightest obtained so far, improving on the bounds obtained in [5] by factors between 1.1 and 1.8.

VII. PARAMETRIZED TESTS OF GRAVITATIONAL-WAVE PROPAGATION

We now place constraints on a phenomenological modification of the GW dispersion relation, i.e., on a possible frequency dependence of the speed of GWs. This modification, introduced in [109] and first applied to LIGO data in [6], is obtained by adding a power-law term in the momentum to the dispersion relation $E^2 = p^2 c^2$ of GWs in GR, giving

$$E^2 = p^2 c^2 + A_\alpha p^\alpha c^\alpha. \quad (2)$$

Here, c is the speed of light, E and p are the energy and momentum of the GWs, and A_α and α are phenomenological parameters. We consider α values from 0 to 4 in steps of 0.5. However, we exclude $\alpha = 2$, where the speed of the GWs is modified in a frequency-independent manner, and therefore gives no observable dephasing.¹⁴ Thus, in all cases except for $\alpha = 0$, we are considering a Lorentz-violating dispersion relation. The group velocity associated with this dispersion relation is $v_g/c = (dE/dp)/c = 1 + (\alpha - 1)A_\alpha E^{\alpha-2}/2 + O(A_\alpha^2)$. The associated length scale is $\lambda_A := hc|A_\alpha|^{1/(\alpha-2)}$, where h is Planck's constant. λ_A gives the scale of modifications to the Newtonian potential (the Yukawa potential for $\alpha = 0$) associated with this dispersion relation.

While Eq. (2) is a purely phenomenological model, it encompasses a variety of more fundamental predictions (at least to leading order) [101,109]. In particular, $A_0 > 0$

¹⁴For a source with an electromagnetic counterpart, A_2 can be constrained by comparison with the arrival time of the photons, as was done with GW170817/GRB 170817A [110].

corresponds to a massive graviton, i.e., the same dispersion as for a massive particle in vacuo [111], with a graviton mass given by $m_g = A_0^{1/2}/c^2$.¹⁵ Furthermore, α values of 2.5, 3, and 4 correspond to the leading predictions of multifractal space-time [112], doubly special relativity [113], and Hořava-Lifshitz [114] and extra dimensional [115] theories, respectively. The standard model extension also gives a leading contribution with $\alpha = 4$ [116], only considering the nonbirefringent terms; our analysis does not allow for birefringence.

In order to obtain a waveform model with which to constrain these propagation effects, we start by assuming that the waveform extracted in the binary's local wave zone (i.e., near to the binary compared to the distance from the binary to Earth, but far from the binary compared to its own size) is well described by a waveform in GR.¹⁶ Since we are able to bound these propagation effects to be very small, we can work to linear order in A_α when computing the effects of this dispersion on the frequency-domain GW phasing,¹⁷ thus obtaining a correction [109] that is added to $\Phi(f)$ in Eq. (1),

$$\delta\Phi_\alpha(f) = \text{sign}(A_\alpha) \begin{cases} \frac{\pi D_L}{\alpha-1} \lambda_{A,\text{eff}}^{\alpha-2} \left(\frac{f}{c}\right)^{\alpha-1}, & \alpha \neq 1 \\ \frac{\pi D_L}{\lambda_{A,\text{eff}}} \ln\left(\frac{\pi G \mathcal{M}^{\text{det}} f}{c^3}\right), & \alpha = 1 \end{cases}. \quad (3)$$

Here, D_L is the binary's luminosity distance, \mathcal{M}^{det} is the binary's detector-frame (i.e., redshifted) chirp mass, and $\lambda_{A,\text{eff}}$ is the effective wavelength parameter used in the sampling, defined as

$$\lambda_{A,\text{eff}} := \left[\frac{(1+z)^{1-\alpha} D_L}{D_\alpha} \right]^{1/(\alpha-2)} \lambda_A. \quad (4)$$

The parameter z is the binary's redshift, and D_α is a distance parameter given by

$$D_\alpha = \frac{(1+z)^{1-\alpha}}{H_0} \int_0^z \frac{(1+\bar{z})^{\alpha-2}}{\sqrt{\Omega_m(1+\bar{z})^3 + \Omega_\Lambda}} d\bar{z}, \quad (5)$$

where $H_0 = 67.90 \text{ km s}^{-1} \text{ Mpc}^{-1}$ is the Hubble constant, and $\Omega_m = 0.3065$ and $\Omega_\Lambda = 0.6935$ are the matter and dark

energy density parameters; these are the TT + lowP + lensing + ext values from [117].¹⁸

The dephasing in Eq. (3) is obtained by treating the gravitational wave as a stream of particles (gravitons), which travel at the particle velocity $v_p/c = pc/E = 1 - A_\alpha E^{\alpha-2}/2 + O(A_\alpha^2)$. There are suggestions to use the particle velocity when considering doubly special relativity, though there are also suggestions to use the group velocity v_g in that case (see, e.g., [119] and references therein for both arguments). However, the group velocity is appropriate for, e.g., multifractal space-time theories (see, e.g., [120]). To convert the bounds presented here to the case where the particles travel at the group velocity, scale the A_α bounds for $\alpha \neq 1$ by factors of $1/(1-\alpha)$. The group velocity calculation gives an unobservable constant phase shift for $\alpha = 1$.

We consider the cases of positive and negative A_α separately, and obtain the results shown in Table IV and Fig. 5 when applying this analysis to the GW events under consideration. While we sample with a flat prior in $\log \lambda_{A,\text{eff}}$, our bounds are given using priors flat in A_α for all results except for the mass of the graviton, where we use a prior flat in the graviton mass. We also show the results from combining together all the signals that satisfy our selection criterion. We are able to combine together the results from different signals with no ambiguity, since the known distance dependence is accounted for in the waveforms.

Figure 6 displays the full A_α posteriors obtained by combining all selected events (using IMRPHENOMPv2 waveforms). To obtain the full A_α posteriors, we combine together the positive and negative A_α results for individual events by weighting by their Bayesian evidences; we then combine the posteriors from individual events. We give the analogous plots for the individual events in Sec. A 4 of the Appendix. The combined positive and negative A_α posteriors are also used to compute the GR quantiles given in Table IV, which give the probability to have $A_\alpha < 0$, where $A_\alpha = 0$ is the GR value. Thus, large or small values of the GR quantile indicate that the distribution is not peaked close to the GR value. For a GR signal, the GR quantile is distributed uniformly in [0,1] for different noise realizations. The GR quantiles we find are consistent with such a uniform distribution. In particular, the (two-tailed) meta p -value for all events and α values obtained using Fisher's method [81] (as in Sec. VA) is 0.9995.

We find that the combined bounds overall improve on those quoted in [6] by roughly the factor of $\sqrt{7/3} \simeq 1.5$

¹⁵Thus, the Yukawa screening length is $\lambda_0 = h/(m_g c)$.

¹⁶This is likely to be a good assumption for $\alpha < 2$, where we constrain λ_A to be much larger than the size of the binary. For $\alpha > 2$, where we constrain λ_A to be much smaller than the size of the binary, one has to posit a screening mechanism in order to be able to assume that the waveform in the binary's local wave zone is well described by GR, as well as for this model to evade Solar System constraints.

¹⁷The dimensionless parameter controlling the size of the linear correction is $A_\alpha f^{\alpha-2}$, which is $\lesssim 10^{-18}$ at the 90% credible level for the events we consider and frequencies up to 1 kHz.

¹⁸We use these values for consistency with the results presented in [14]. If we instead use the more recent results from [118], specifically the TT, TE, EE + lowE + lensing + BAO values used for comparison in [14], then there are very minor changes to the results presented in this section. For instance, the upper bounds in Table IV change by at most $\sim 0.1\%$.

TABLE IV. 90% credible level upper bounds on the graviton mass m_g and the absolute value of the modified dispersion relation parameter A_α , as well as the GR quantiles Q_{GR} . The $<$ and $>$ labels denote the bounds for $A_\alpha < 0$ and > 0 , respectively, and we have defined the dimensionless quantity $\bar{A}_\alpha := A_\alpha/eV^{2-\alpha}$. Events with names in boldface are used to obtain the combined results.

| Event | m_g | $ \bar{A}_0 $ | | $ \bar{A}_{0.5} $ | | $ \bar{A}_1 $ | | $ \bar{A}_{1.5} $ | | $ \bar{A}_{2.5} $ | | $ \bar{A}_3 $ | | $ \bar{A}_{3.5} $ | | $ \bar{A}_4 $ | | | | | | | | | |
|-----------------|-----------------------------|---------------|------|-------------------|------|---------------|-----------------|-------------------|-----|-------------------|------|---------------|-----------------|-------------------|------|-----------------|-----|-----|-----------------|-----|-----|-----|-----|-----|-----|
| | $[10^{-23} \text{ eV}/c^2]$ | $<$ | $>$ | Q_{GR} | $<$ | $>$ | Q_{GR} | $<$ | $>$ | Q_{GR} | $<$ | $>$ | Q_{GR} | $<$ | $>$ | Q_{GR} | $<$ | $>$ | Q_{GR} | | | | | | |
| GW150914 | 9.9 | 1.4 | 1.1 | 71 | 5.9 | 4.9 | 57 | 5.5 | 3.5 | 74 | 3.2 | 2.1 | 74 | 2.4 | 2.1 | 50 | 17 | 19 | 37 | 11 | 20 | 42 | 7.7 | 9.8 | 52 |
| GW151012 | 17 | 3.8 | 3.5 | 40 | 3.6 | 11 | 35 | 6.6 | 9.5 | 41 | 1.9 | 2.5 | 46 | 2.8 | 1.5 | 56 | 21 | 9.7 | 56 | 18 | 15 | 61 | 14 | 6.7 | 58 |
| GW151226 | 29 | 7.1 | 9.3 | 21 | 8.1 | 21 | 10 | 13 | 13 | 26 | 3.4 | 3.3 | 28 | 3.4 | 2.1 | 68 | 22 | 9.7 | 61 | 14 | 6.1 | 58 | 19 | 5.4 | 72 |
| GW170104 | 9.2 | 2.5 | 0.99 | 62 | 4.2 | 2.4 | 72 | 7.0 | 2.9 | 76 | 1.9 | 0.80 | 83 | 1.1 | 2.8 | 23 | 10 | 13 | 35 | 6.4 | 10 | 37 | 6.5 | 8.7 | 43 |
| GW170608 | 30 | 13 | 9.2 | 49 | 22 | 8.8 | 68 | 15 | 28 | 49 | 3.1 | 3.8 | 64 | 3.3 | 2.1 | 49 | 9.8 | 8.3 | 46 | 87 | 8.0 | 46 | 30 | 3.7 | 38 |
| GW170729 | 7.4 | 0.29 | 0.64 | 17 | 0.93 | 1.1 | 26 | 2.1 | 4.5 | 16 | 0.79 | 1.5 | 18 | 4.2 | 1.4 | 94 | 36 | 8.6 | 96 | 26 | 8.9 | 94 | 43 | 7.1 | 95 |
| GW170809 | 9.3 | 1.4 | 1.2 | 64 | 2.5 | 2.5 | 49 | 11 | 5.8 | 49 | 1.4 | 2.3 | 37 | 3.8 | 1.3 | 79 | 22 | 6.9 | 81 | 18 | 6.2 | 78 | 13 | 6.5 | 82 |
| GW170814 | 8.5 | 4.0 | 1.1 | 94 | 5.2 | 1.8 | 92 | 15 | 5.2 | 93 | 3.0 | 1.3 | 96 | 1.3 | 3.9 | 5.7 | 7.4 | 25 | 6.2 | 5.4 | 29 | 7.5 | 4.2 | 13 | 9.6 |
| GW170818 | 7.2 | 1.4 | 0.66 | 74 | 2.5 | 1.9 | 80 | 4.9 | 4.3 | 73 | 1.7 | 0.67 | 79 | 1.4 | 3.4 | 28 | 17 | 15 | 41 | 19 | 7.9 | 73 | 12 | 9.0 | 49 |
| GW170823 | 6.3 | 1.2 | 0.49 | 61 | 1.1 | 1.6 | 51 | 2.7 | 2.3 | 49 | 0.99 | 1.2 | 46 | 2.5 | 1.3 | 53 | 11 | 16 | 41 | 8.8 | 11 | 37 | 14 | 11 | 46 |
| Combined | 4.7 | 0.80 | 0.34 | 79 | 1.2 | 0.70 | 73 | 2.5 | 1.2 | 70 | 0.70 | 0.37 | 86 | 0.50 | 0.80 | 28 | 2.9 | 3.7 | 25 | 2.0 | 3.7 | 35 | 1.4 | 2.3 | 34 |

expected from including more events, with the bounds for some quantities improving by up to a factor of 2.5, due to the inclusion of several more massive and distant systems in the sample.¹⁹ These massive and distant systems, notably GW170823 (and GW170729, which is not included in the combined results), generally give the best individual bounds, particularly for small values of α , where the dephasing is largest at lower frequencies. Closer and less massive systems such as GW151226 and GW170608 provide weaker bounds, overall. However, their bounds can be comparable to those of the more massive, distant events for larger values of α . The lighter systems have more power at higher frequencies where the dephasing from the modified dispersion is larger for larger values of α .

The new combined bound on the mass of the graviton of $m_g \leq 4.7 \times 10^{-23} \text{ eV}/c^2$ is a factor of 1.6 improvement on the one presented in [6]. It is also a small improvement on the bound of $m_g \leq 6.76 \times 10^{-23} \text{ eV}/c^2$ (90% confidence level) obtained from Solar System ephemerides in [121].²⁰ However, these bounds are complementary, since the GW bound comes from the radiative sector, while the Solar System bound considers the static modification to the

Newtonian potential. See, e.g., [123] for a review of bounds on the mass of the graviton.

We find that the posterior on A_α peaks away from 0 in some cases (illustrated in Sec. A 4 of the Appendix), and the GR quantile is in one of the tails of the distribution. This feature is expected for a few out of ten events, simply from Gaussian noise fluctuations. We have performed

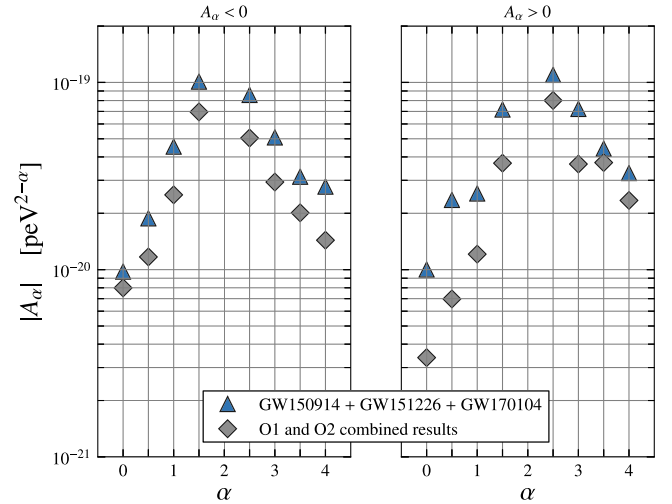


FIG. 5. 90% credible upper bounds on the absolute value of the modified dispersion relation parameter A_α . We show results for positive and negative values of A_α separately. Specifically, we give the updated versions of the results from combining together GW150914, GW151226, and GW170104 (first given in [6]), as well as the results from combining together all the events meeting our significance threshold for combined results (see Table I). Picoelectronvolts (peV) provide a convenient scale, because $1 \text{ peV} \simeq h \times 250 \text{ Hz}$, where 250 Hz is roughly around the most sensitive frequencies of the LIGO and Virgo instruments.

¹⁹While the results in [6] were affected by a slight normalization issue, and also had insufficiently fine binning in the computation of the upper bounds, we find improvements of up to a factor of 3.4 when comparing to the combined GW150914 + GW151226 + GW170104 bounds we compute here.

²⁰The much stronger bound in [122] is deduced from a postfit analysis (i.e., using the residuals of a fit to Solar System ephemerides performed without including the effects of a massive graviton). It may therefore overestimate Solar System constraints, as is indeed seen to be the case in [121].

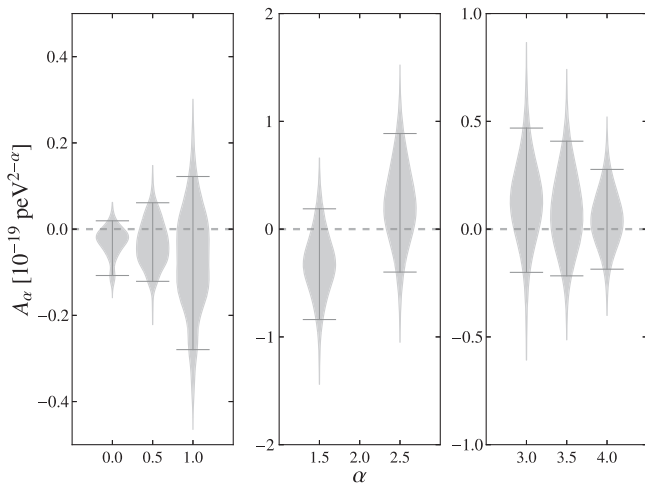


FIG. 6. Violin plots of the full posteriors on the modified dispersion relation parameter A_α calculated from the combined events, with the 90% credible interval around the median indicated.

simulations of 100 GR sources with source-frame component masses lying between 25 and 45 M_\odot , isotropically distributed spins with dimensionless magnitudes up to 0.99, and at luminosity distances between 500 and 800 Mpc. These simulations used the waveform model IMRPHENOMPv2 and considered the Advanced LIGO and Virgo network, using Gaussian noise with the detectors' design sensitivity power spectral densities. We found that in about 20%–30% of cases, the GR quantile lies in the tails of the distribution (i.e., <10% or >90%), when the sources injected are analyzed using the same waveform model (IMRPHENOMPv2).

In order to assess the impact of waveform systematics, we also analyze some events using the aligned-spin SEOBNRv4 model. We consider GW170729 and GW170814 in depth in this study because the GR quantiles of the IMRPHENOMPv2 results lie in the tails of the distributions, and find that the 90% upper bounds and GR quantiles presented in Table IV differ by at most a factor of 2.3 for GW170729 and 1.5 for GW170814 when computed using the SEOBNRv4 model. These results are presented in Sec. A 4 of the Appendix.

There are also uncertainties in the determination of the 90% bounds due to the finite number of samples and the long tails of the distributions. As in Ref. [6], we quantify this uncertainty using Bayesian bootstrapping [124]. We use 1000 bootstrap realizations for each value of α and sign of A_α , obtaining a distribution of 90% bounds on A_α . We consider the 90% credible interval of this distribution and find that its width is <30% of the values for the 90% bounds on A_α given in Table IV for all but 10 of the 160 cases we consider (counting positive and negative A_α cases separately). For GW170608, $A_4 < 0$, the width of the 90% credible interval from bootstrapping is 91% of the value in Table IV. This ratio is $\leq 47\%$ for all the remaining cases. Thus, there are a few cases where the bootstrapping

uncertainty in the bound on A_α is large, but for most cases, this is not a substantial uncertainty.

VIII. POLARIZATIONS

Generic metric theories of gravity may allow up to six polarizations of gravitational waves [125]: two tensor modes (helicity ± 2), two vector modes (helicity ± 1), and two scalar modes (helicity 0). Of these, only the two tensor modes (+ and \times) are permitted in GR. We may attempt to reconstruct the polarization content of a passing GW using a network of detectors [1,126–129]. This is possible because instruments with different orientations will respond differently to signals from a given sky location depending on their polarization. In particular, the strain signal in detector I can be written as $h_I(t) = \sum_A F^A_I h_A(t)$, with F^A_I being the detector's response function and $h_A(t)$ the A -polarized part of the signal [1,130].

In order to fully disentangle the polarization content of a transient signal, at least five detectors are needed to break all degeneracies [126].²¹ This limits the polarization measurements that are currently feasible. In spite of this, we may extract some polarization information from signals detected with both LIGO detectors and Virgo [129]. This was done previously with GW170814 and GW170817 to provide evidence that GWs are tensor polarized, instead of fully vector or fully scalar [7,8]. Besides GW170814, there are three binary black hole events that were detected with the full network (GW170729, GW170809, and GW170818). Of these events, only GW170818 has enough SNR and is sufficiently well localized to provide any relevant information (cf. Fig. 8 in [14]). The Bayes factors (marginalized likelihood ratios) obtained in this case are 12 ± 3 for tensor vs vector and 407 ± 100 for tensor vs scalar, where the error corresponds to the uncertainty due to discrete sampling in the evidence computations. These values are comparable to those from GW170814, for which the latest recalibrated and cleaned data (cf. Sec. II) yield Bayes factors of 30 ± 4 and 220 ± 27 for tensor vs vector and scalar, respectively.²² Values from these binary black holes are many orders of magnitude weaker than those obtained from GW170817, where we benefited from the precise sky localization provided by an electromagnetic counterpart [8].

IX. CONCLUSIONS AND OUTLOOK

We have presented the results from various tests of GR performed using the binary black hole signals from the

²¹Differential-arm detectors are only sensitive to the traceless scalar mode, meaning we can only hope to distinguish five, not six, polarizations.

²²These values are less stringent than those previously published in [7]. This is solely due to the change in data, which impacted the sky locations inferred under the non-GR hypotheses.

catalog GWTC-1 [9], i.e., those observed by Advanced LIGO and Advanced Virgo during the first two observing runs of the advanced detector era. These tests, which are among the first tests of GR in the highly relativistic, nonlinear regime of strong gravity, do not reveal any inconsistency of our data with the predictions of GR. We have presented full results on four tests of the consistency of the data with gravitational waveforms from binary black hole systems as predicted by GR. The first two of these tests check the self-consistency of our analysis. One checks that the residual remaining after subtracting the best-fit waveform is consistent with detector noise. The other checks that the final mass and spin inferred from the low- and high-frequency parts of the signal are consistent. The third and fourth tests introduce parametrized deviations in the waveform model and check that these deviations are consistent with their GR value of 0. In one test, these deviations are completely phenomenological modifications of the coefficients in a waveform model, including the post-Newtonian coefficients. In the other test, the deviations are those arising from the propagation of GWs with a modified dispersion relation, which includes the dispersion due to a massive graviton as a special case. In addition, we also check whether the observed polarizations are consistent with being purely tensor modes (as expected in GR) as opposed to purely scalar modes or vector modes.

We present results from all binary black hole events that are detected with a false-alarm rate better than $(1 \text{ yr})^{-1}$. This includes results from the reanalysis of some of the events which were published earlier [4–7], with better calibration and data quality. Assuming that the parameters that describe deviations from GR take values that are independent of source properties, we can combine results from multiple events. We choose to combine results only from highly significant events, detected with a false-alarm rate better than $(1000 \text{ yr})^{-1}$ in both modeled searches. Combining together these results has allowed us to significantly reduce the statistical errors on constraints on deviations from GR predictions, as compared to those from individual events. The combined constraints presented here improve our previously presented constraints by factors of 1.1 to 2.5, with the largest improvements obtained for certain cases of the modified dispersion test. Notable constraints include that on the graviton’s mass $m_g \leq 4.7 \times 10^{-23} \text{ eV}/c^2$ (an improvement of a factor of 1.6 over previously presented constraints) and the first constraint on the -1 PN coefficient obtained from binary black holes.

With the expected observations of additional binary black hole merger events in the upcoming LIGO/Virgo observing runs [14,131], the statistical errors of the combined results will soon decrease significantly. A number of potential sources of systematic errors (due to imperfect modeling of GR waveforms, calibration uncertainties, noise artifacts, etc.) need to be understood for future high-precision tests of strong gravity using GW

observations. However, work to improve the analysis on all these fronts is well underway, for instance the inclusion of full spin-precession dynamics [24,66–69], nonquadrupolar modes [68,69,72–74], and eccentricity [52–59] in waveform models, as well as analyses that compare directly with numerical relativity waveforms [132,133]. Additionally, a new, more flexible parameter estimation infrastructure is currently being developed [134], and this will allow for improvements in, e.g., the treatment of calibration uncertainties or PSD estimation to be incorporated more easily. We thus expect that tests of general relativity using the data from upcoming observing runs will be able to take full advantage of the increased sensitivity of the detectors.

ACKNOWLEDGMENTS

The authors gratefully acknowledge the support of the United States National Science Foundation (NSF) for the construction and operation of the LIGO Laboratory and Advanced LIGO as well as the Science and Technology Facilities Council (STFC) of the United Kingdom, the Max-Planck-Society (MPS), and the State of Niedersachsen/Germany for support of the construction of Advanced LIGO and construction and operation of the GEO600 detector. Additional support for Advanced LIGO was provided by the Australian Research Council. The authors gratefully acknowledge the Italian Istituto Nazionale di Fisica Nucleare (INFN), the French Centre National de la Recherche Scientifique (CNRS) and the Foundation for Fundamental Research on Matter supported by the Netherlands Organisation for Scientific Research, for the construction and operation of the Virgo detector and the creation and support of the EGO consortium. The authors also gratefully acknowledge research support from these agencies as well as by the Council of Scientific and Industrial Research of India, the Department of Science and Technology, India, the Science & Engineering Research Board (SERB), India, the Ministry of Human Resource Development, India, the Spanish Agencia Estatal de Investigación, the Vicepresidència i Conselleria d’Innovació, Recerca i Turisme and the Conselleria d’Educació i Universitat del Govern de les Illes Balears, the Conselleria d’Educació, Investigació, Cultura i Esport de la Generalitat Valenciana, the National Science Centre of Poland, the Swiss National Science Foundation (SNSF), the Russian Foundation for Basic Research, the Russian Science Foundation, the European Commission, the European Regional Development Funds (ERDF), the Royal Society, the Scottish Funding Council, the Scottish Universities Physics Alliance, the Hungarian Scientific Research Fund (OTKA), the Lyon Institute of Origins (LIO), the Paris Île-de-France Region, the National Research, Development and Innovation Office Hungary (NKFIH), the National Research Foundation of Korea, Industry Canada and the Province of Ontario through the Ministry of Economic Development and Innovation, the

Natural Science and Engineering Research Council Canada, the Canadian Institute for Advanced Research, the Brazilian Ministry of Science, Technology, Innovations, and Communications, the International Center for Theoretical Physics South American Institute for Fundamental Research (ICTP-SAIFR), the Research Grants Council of Hong Kong, the National Natural Science Foundation of China (NSFC), the Leverhulme Trust, the Research Corporation, the Ministry of Science and Technology (MOST), Taiwan and the Kavli Foundation. The authors gratefully acknowledge the support of the NSF, STFC, MPS, INFN, CNRS, and the State of Niedersachsen/Germany for provision of computational resources. The authors thank Clifford Will and Nicolás Yunes for useful discussions.

APPENDIX: INDIVIDUAL RESULTS AND SYSTEMATIC STUDIES

In the main body of the paper, for most analyses, we present only the combined results from all events. Here we present the posteriors from various tests obtained from individual events. In addition, we offer a limited discussion on systematic errors in the analysis, due to the specific choice of a GR waveform approximant.

1. Residuals test

As mentioned in Sec. VA, the residuals test is sensitive to all kinds of disagreement between the best-fit GR-based waveform and the data. This is true whether the disagreement is due to actual deviations from GR or more mundane reasons, like physics missing from our waveform models (e.g., higher-order modes). Had we found compelling evidence of coherent power in the residuals that could not be explained by instrumental noise, further investigations would be required to determine its origin. However, given our null result, we can simply state that we find no evidence for shortcomings in the best-fit waveform, neither from deviations from GR nor modeling systematics.

As the sensitivity of the detectors improves, the issue of systematics will become increasingly more important. To address this, future versions of this test will be carried out by subtracting a best-fit waveform produced with more accurate GR-based models, including numerical relativity.

2. Inspiral-merger-ringdown consistency test

In order to gauge the systematic errors in the IMR consistency test results due to imperfect waveform modeling, we have also estimated the posteriors of the deviation parameters $\Delta M_f/\bar{M}_f$ and $\Delta a_f/\bar{a}_f$ using the effective-one-body based waveform family SEOBNRv4 that models binary black holes with nonprecessing spins. This analysis uses the same priors as used in the main analysis presented in Sec. VB, except that spins are assumed to be aligned/antialigned with the orbital angular momentum of the

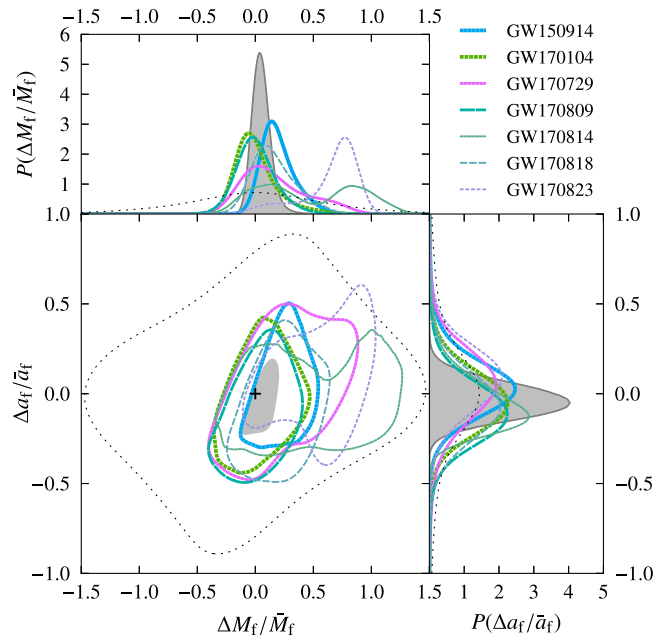


FIG. 7. Same as Fig. 2, except that the posteriors are computed using the nonprecessing-spin SEOBNRv4 waveforms.

binary. The resulting posteriors are presented in Fig. 7 and are broadly consistent with the posteriors using IMRPHENOMPv2 presented in Fig. 2. The differences in the posteriors of some of the individual events are not surprising, due to the different assumptions on the spins. For all events, the GR value is recovered in the 90% credible region of the posteriors.

3. Parametrized tests of gravitational-wave generation

Figures 8 and 9 report the parametrized tests of waveform deviations for the individual events, augmenting the results shown in Fig. 3. A statistical summary of the posterior probability density functions, showing median and symmetric 90% credible level bounds for the measured parameters is given in Table V. Sources with low SNR in the inspiral regime yield uninformative posterior distributions on $\delta\hat{\phi}_i$. These sources are the ones farther away and with higher mass, which merge at lower frequencies. For instance, although GW170823 has a total mass close to that of GW150914, being much farther away (and redshifted to lower frequencies) makes it a low-SNR event, leaving very little information content in the inspiral regime. The same holds true for GW170729, which has a larger mass. Conversely, low-mass events like GW170608, having a significantly larger SNR in the inspiral regime and many more cycles in the frequency band, provide very strong constraints in the $\delta\hat{\phi}_i$ parameters (especially the low-order ones) while providing no useful constraints in the merger-ringdown parameters $\delta\hat{a}_i$.

The choice of the SNR > 6 threshold explained in Sec. III ensures that most analyses are informative. However, this is not true in all cases, as not all parameters

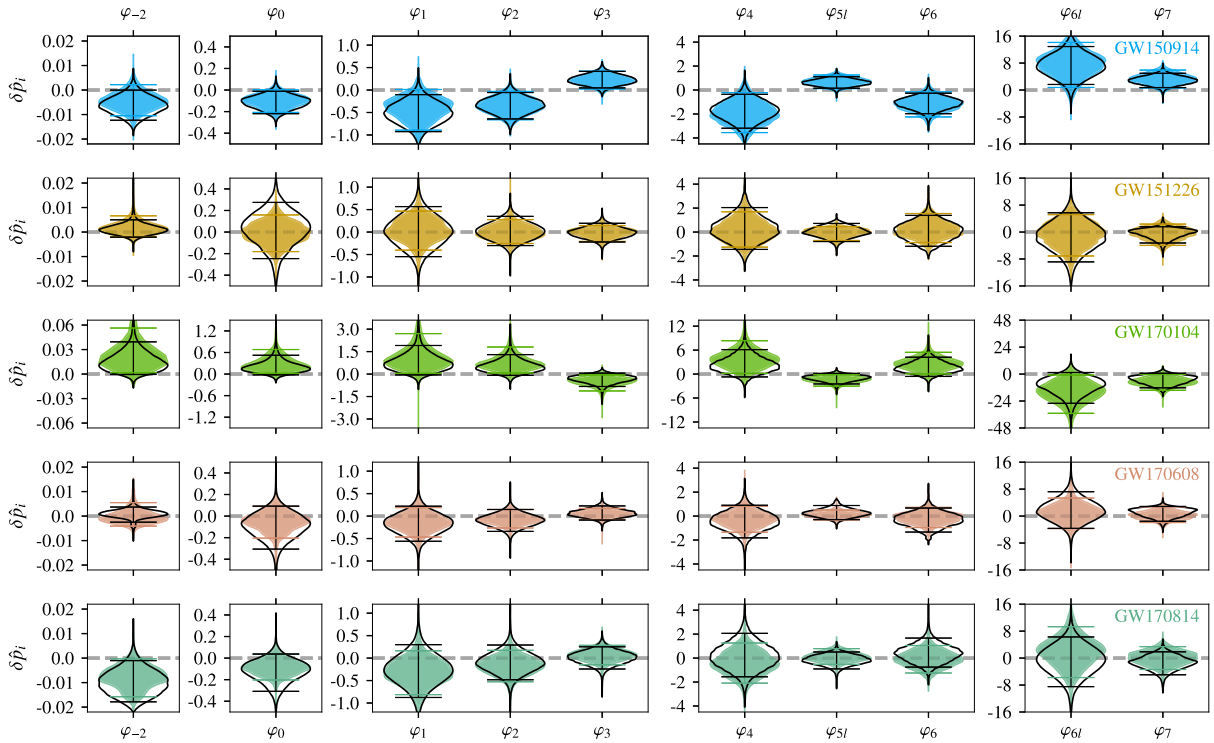


FIG. 8. Violin plots showing inspiral $\delta\hat{p}_i$ posteriors for the individual binary black hole events of GWTC-1 [14] outlined in Sec. III (see the PI column of Table I), using IMRPHENOMPv2 (shaded regions) and SEOBNRv4 (black solid lines). Thin horizontal lines indicate the 90% credible intervals, which show an overall statistical consistency with GR (dashed grey line).

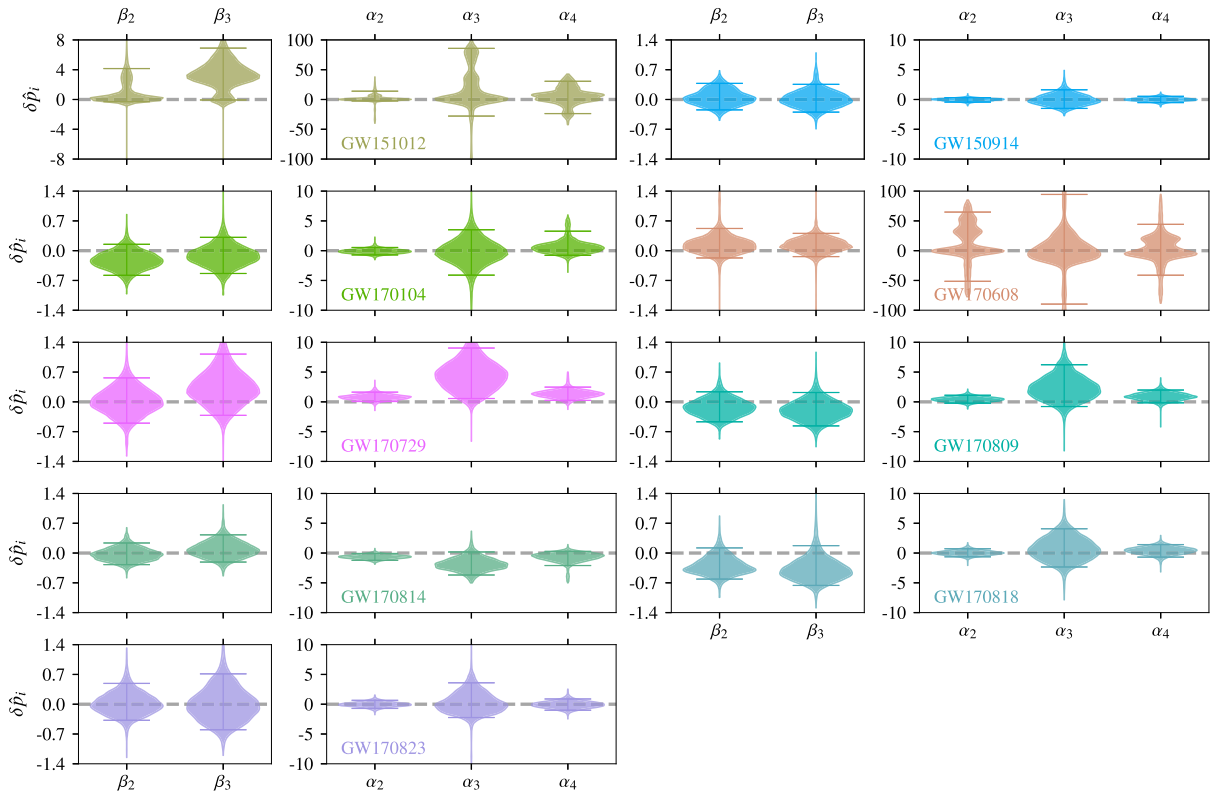


FIG. 9. Violin plots showing postinspiral $\delta\hat{p}_i$ posteriors for the individual binary black hole events of GWTC-1 [14] outlined in Sec. III (see the PPI column of Table I), using IMRPHENOMPv2. Thin horizontal lines indicate the 90% credible intervals, which show an overall statistical consistency with GR (dashed grey line).

TABLE V. Median value and symmetric 90% credible level bounds of the waveform parameters $\delta\hat{\rho}_i$, as well as the GR quantiles Q_{GR} . For the inspiral parameters, we show results in pairs of rows for when the data from individual events are analyzed using IMRPHENOMPv2 (P) and SEOBNRv4 (S), while for the postinspiral phenomenological parameters, results are obtained only for IMRPHENOMPv2.

| Parameter | Model | GW150914 | | GW151226 | | GW170104 | | GW170608 | | GW170814 | |
|-----------------------------------------------|-------|-----------------------------------------|--------------|-----------------------------------------|--------------|-----------------------------------------|--------------|-----------------------------------------|--------------|-----------------------------------------|--------------|
| | | \tilde{X}_{\pm} | Q_{GR} [%] | \tilde{X}_{\pm} | Q_{GR} [%] | \tilde{X}_{\pm} | Q_{GR} [%] | \tilde{X}_{\pm} | Q_{GR} [%] | \tilde{X}_{\pm} | Q_{GR} [%] |
| $\delta\hat{\rho}_{-2}$ [10 ⁻²] | P | -0.46 ^{+0.68} _{-0.59} | 88 | 0.14 ^{+0.52} _{-0.35} | 27 | 2.0 ^{+3.6} _{-1.9} | 3 | -0.06 ^{+0.61} _{-0.35} | 60 | -0.76 ^{+0.74} _{-0.81} | 96 |
| | S | -0.63 ^{+0.62} _{-0.61} | 95 | 0.10 ^{+0.40} _{-0.31} | 30 | 1.4 ^{+2.6} _{-1.4} | 5.9 | 0.10 ^{+0.27} _{-0.34} | 26 | -0.99 ^{+0.89} _{-0.79} | 97 |
| $\delta\hat{\rho}_0$ [10 ⁻¹] | P | -1.0 ^{+1.0} _{-1.1} | 95 | -0.1 ^{+1.7} _{-1.7} | 53 | 2.5 ^{+4.3} _{-2.3} | 3.1 | -0.5 ^{+1.4} _{-1.6} | 73 | -0.8 ^{+1.2} _{-1.2} | 88 |
| | S | -1.1 ^{+1.0} _{-1.1} | 97 | 0.3 ^{+2.4} _{-2.8} | 41 | 1.8 ^{+3.5} _{-2.0} | 7.3 | -0.9 ^{+1.8} _{-2.2} | 77 | -1.1 ^{+1.5} _{-2.0} | 89 |
| $\delta\hat{\rho}_1$ [10 ⁰] | P | -0.39 ^{+0.40} _{-0.50} | 95 | 0.03 ^{+0.43} _{-0.44} | 45 | 1.0 ^{+1.7} _{-0.9} | 4.1 | -0.14 ^{+0.33} _{-0.33} | 76 | -0.31 ^{+0.47} _{-0.50} | 86 |
| | S | -0.51 ^{+0.41} _{-0.41} | 98 | 0.02 ^{+0.55} _{-0.56} | 48 | 0.7 ^{+1.2} _{-0.8} | 6.6 | -0.16 ^{+0.38} _{-0.40} | 77 | -0.27 ^{+0.57} _{-0.61} | 79 |
| $\delta\hat{\rho}_2$ [10 ⁰] | P | -0.35 ^{+0.32} _{-0.31} | 97 | -0.01 ^{+0.29} _{-0.24} | 52 | 0.7 ^{+1.1} _{-0.6} | 3.5 | -0.07 ^{+0.21} _{-0.20} | 72 | -0.17 ^{+0.34} _{-0.36} | 80 |
| | S | -0.34 ^{+0.28} _{-0.30} | 97 | 0.02 ^{+0.33} _{-0.32} | 47 | 0.47 ^{+0.83} _{-0.56} | 8.6 | -0.09 ^{+0.24} _{-0.25} | 75 | -0.10 ^{+0.39} _{-0.38} | 67 |
| $\delta\hat{\rho}_3$ [10 ⁻¹] | P | 2.2 ^{+2.0} _{-1.9} | 3.4 | -0.1 ^{+1.5} _{-2.0} | 54 | -4.8 ^{+4.2} _{-6.5} | 97 | 0.5 ^{+1.2} _{-1.2} | 26 | 0.7 ^{+2.1} _{-2.2} | 30 |
| | S | 2.2 ^{+2.0} _{-1.8} | 1.8 | -0.2 ^{+2.0} _{-2.0} | 55 | -3.2 ^{+3.8} _{-5.2} | 91 | 0.6 ^{+1.6} _{-1.4} | 26 | 0.1 ^{+2.4} _{-2.4} | 48 |
| $\delta\hat{\rho}_4$ [10 ⁰] | P | -1.9 ^{+1.7} _{-1.6} | 97 | 0.1 ^{+1.6} _{-1.3} | 47 | 3.7 ^{+4.6} _{-3.6} | 4.2 | -0.3 ^{+1.1} _{-1.1} | 67 | -0.5 ^{+1.7} _{-1.6} | 67 |
| | S | -1.7 ^{+1.3} _{-1.5} | 98 | 0.2 ^{+1.8} _{-1.6} | 41 | 2.2 ^{+3.9} _{-2.9} | 10 | -0.4 ^{+1.3} _{-1.4} | 70 | 0.1 ^{+1.9} _{-1.7} | 45 |
| $\delta\hat{\rho}_5^{(I)}$ [10 ⁰] | P | 0.70 ^{+0.56} _{-0.58} | 2.2 | -0.03 ^{+0.49} _{-0.67} | 54 | -1.4 ^{+1.3} _{-1.6} | 97 | 0.09 ^{+0.42} _{-0.42} | 36 | 0.10 ^{+0.69} _{-0.62} | 40 |
| | S | 0.61 ^{+0.49} _{-0.45} | 1.5 | 0.00 ^{+0.71} _{-0.77} | 50 | -1.0 ^{+1.1} _{-1.5} | 92 | 0.25 ^{+0.62} _{-0.54} | 23 | -0.16 ^{+0.66} _{-0.72} | 64 |
| $\delta\hat{\rho}_6$ [10 ⁰] | P | -1.2 ^{+1.0} _{-1.1} | 97 | 0.2 ^{+1.3} _{-1.1} | 40 | 2.6 ^{+2.9} _{-2.5} | 4.7 | -0.11 ^{+0.84} _{-0.84} | 59 | -0.1 ^{+1.2} _{-1.1} | 56 |
| | S | -1.07 ^{+0.80} _{-0.92} | 99 | 0.1 ^{+1.3} _{-1.3} | 45 | 1.6 ^{+2.7} _{-2.1} | 11 | -0.3 ^{+1.0} _{-1.0} | 68 | 0.4 ^{+1.3} _{-1.1} | 29 |
| $\delta\hat{\rho}_6^{(I)}$ [10 ¹] | P | 0.78 ^{+0.63} _{-0.70} | 3.5 | -0.05 ^{+0.56} _{-0.66} | 55 | -1.6 ^{+1.5} _{-1.9} | 96 | 0.09 ^{+0.44} _{-0.47} | 36 | 0.20 ^{+0.73} _{-0.78} | 32 |
| | S | 0.72 ^{+0.57} _{-0.55} | 1.8 | -0.13 ^{+0.70} _{-0.76} | 61 | -1.0 ^{+1.1} _{-1.6} | 92 | 0.15 ^{+0.57} _{-0.52} | 31 | -0.07 ^{+0.69} _{-0.78} | 56 |
| $\delta\hat{\rho}_7$ [10 ⁰] | P | 3.2 ^{+2.7} _{-2.6} | 2.2 | -0.4 ^{+2.8} _{-3.5} | 58 | -7.0 ^{+6.9} _{-7.4} | 95 | 0.3 ^{+2.5} _{-2.2} | 42 | 0.2 ^{+3.2} _{-3.5} | 47 |
| | S | 2.8 ^{+2.1} _{-2.0} | 1.3 | -0.1 ^{+1.7} _{-3.1} | 54 | -4.8 ^{+5.4} _{-7.2} | 93 | 1.1 ^{+1.8} _{-2.7} | 23 | -1.2 ^{+3.1} _{-3.2} | 73 |
| $\delta\hat{\beta}_2$ [10 ⁰] | P | 0.03 ^{+0.35} _{-0.28} | 43 | ... | ... | -0.23 ^{+0.38} _{-0.35} | 85 | 0.13 ^{+0.40} _{-0.30} | 25 | -0.04 ^{+0.28} _{-0.23} | 61 |
| $\delta\hat{\beta}_3$ [10 ⁰] | P | 0.00 ^{+0.36} _{-0.30} | 50 | ... | ... | -0.13 ^{+0.44} _{-0.41} | 71 | 0.12 ^{+0.28} _{-0.26} | 21 | 0.07 ^{+0.35} _{-0.29} | 35 |
| $\delta\hat{\alpha}_2$ [10 ⁰] | P | -0.02 ^{+0.34} _{-0.42} | 54 | ... | ... | -0.13 ^{+0.67} _{-0.58} | 64 | 3 ⁺⁶² ₋₅₅ | 40 | -0.64 ^{+0.57} _{-0.59} | 97 |
| $\delta\hat{\alpha}_3$ [10 ⁰] | P | -0.1 ^{+1.7} _{-1.4} | 55 | ... | ... | -0.3 ^{+3.8} _{-3.8} | 55 | -1 ⁺⁹⁵ ₋₈₉ | 52 | -1.9 ^{+2.1} _{-1.8} | 93 |
| $\delta\hat{\alpha}_4$ [10 ⁰] | P | -0.01 ^{+0.54} _{-0.51} | 52 | ... | ... | 0.5 ^{+2.8} _{-1.3} | 28 | -1 ⁺⁴⁵ ₋₄₁ | 51 | -0.6 ^{+0.9} _{-1.5} | 85 |

| Parameter | Model | GW151012 | | GW170729 | | GW170809 | | GW170818 | | GW170823 | |
|-------------------------------------------|-------|-------------------------------------|--------------|----------------------------------------|--------------|-----------------------------------------|--------------|-----------------------------------------|--------------|-----------------------------------------|--------------|
| | | \tilde{X}_{\pm} | Q_{GR} [%] | \tilde{X}_{\pm} | Q_{GR} [%] | \tilde{X}_{\pm} | Q_{GR} [%] | \tilde{X}_{\pm} | Q_{GR} [%] | \tilde{X}_{\pm} | Q_{GR} [%] |
| $\delta\hat{\beta}_2$ [10 ⁰] | P | 0.3 ^{+3.8} _{-0.6} | 24 | 0.01 ^{+0.56} _{-0.51} | 49 | -0.13 ^{+0.37} _{-0.33} | 74 | -0.32 ^{+0.44} _{-0.29} | 89 | 0.00 ^{+0.49} _{-0.38} | 50 |
| $\delta\hat{\beta}_3$ [10 ⁰] | P | 3.3 ^{+3.6} _{-3.4} | 5.6 | 0.31 ^{+0.81} _{-0.63} | 21 | -0.20 ^{+0.42} _{-0.36} | 80 | -0.41 ^{+0.58} _{-0.36} | 90 | -0.02 ^{+0.74} _{-0.57} | 52 |
| $\delta\hat{\alpha}_2$ [10 ⁰] | P | 0 ⁺¹⁴ ₋₃ | 37 | 0.78 ^{+0.85} _{-0.73} | 4 | 0.42 ^{+0.69} _{-0.64} | 14 | 0.01 ^{+0.71} _{-0.65} | 49 | -0.04 ^{+0.70} _{-0.66} | 55 |
| $\delta\hat{\alpha}_3$ [10 ⁰] | P | 5 ⁺⁸¹ ₋₃₃ | 29 | 4.4 ^{+4.6} _{-3.8} | 2.1 | 2.2 ^{+4.0} _{-3.0} | 12 | 0.6 ^{+3.5} _{-2.9} | 38 | 0.1 ^{+3.5} _{-2.3} | 49 |
| $\delta\hat{\alpha}_4$ [10 ⁰] | P | 6 ⁺²⁴ ₋₃₀ | 33 | 1.3 ^{+1.2} _{-1.1} | 2.2 | 0.9 ^{+1.1} _{-1.0} | 7.6 | 0.4 ^{+1.0} _{-1.1} | 26 | -0.09 ^{+0.97} _{-0.92} | 56 |

are as easily determined from the data (cf. the good constraints one obtains on the chirp mass with the much weaker constraints on the mass ratio). The two events for which the SNR threshold is insufficient are GW151012 and GW170608, where some postinspiral parameters are largely unconstrained. The postinspiral regime is itself divided into the intermediate and merger-ringdown regimes, and for both these events we find the intermediate

regime parameters ($\delta\hat{\beta}_i$) to be informative; however, the merger-ringdown $\delta\hat{\alpha}_3$ for GW170608 and all $\delta\hat{\alpha}_i$ for GW151012 extend across the entire prior range considered in the analyses, far beyond the range constrained by other events (as can be seen in Fig. 9). Although we use the results from GW170608 $\delta\hat{\alpha}_i$ for combining posteriors in Fig. 3, the combined bounds remain unaffected by adding these results. For future tests, a more discerning threshold

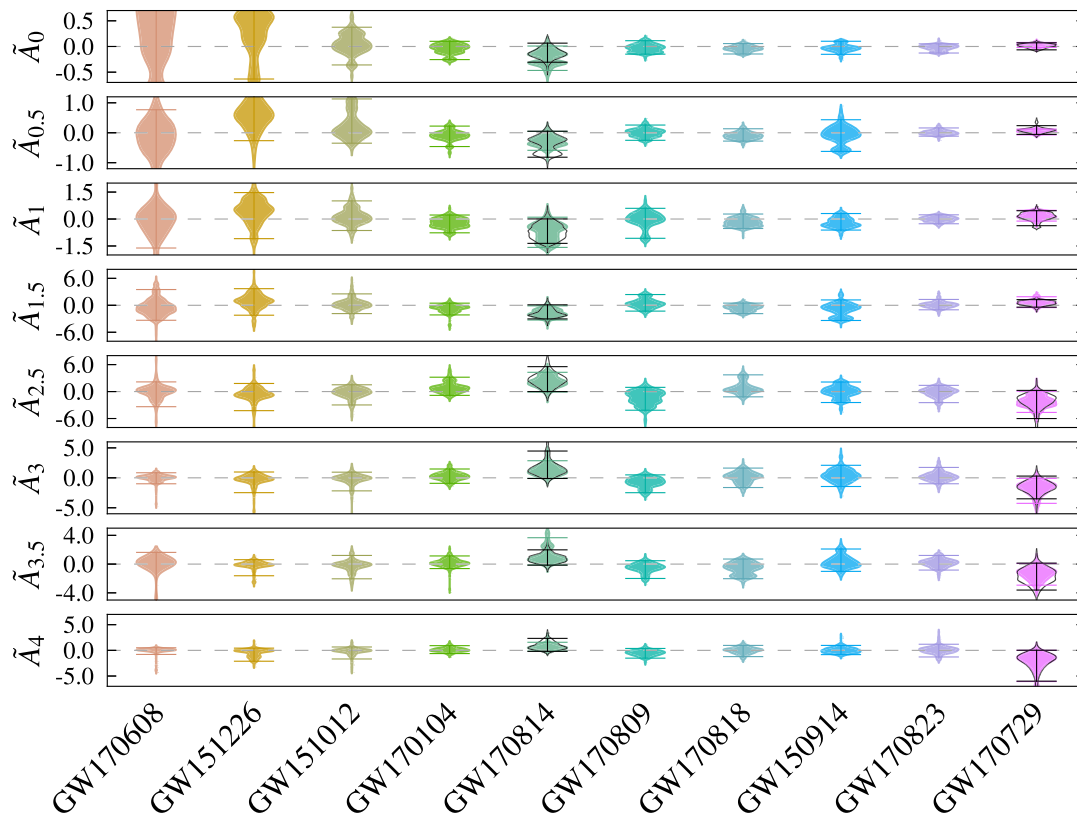


FIG. 10. Violin plots of the full posteriors for the modified dispersion relation parameter A_α for the individual binary black hole events of GWTC-1 [14], with the 90% credible interval around the median indicated. The events are ordered left to right by increasing median total mass. The filled violins are the IMRPHENOMPv2 results, while the unfilled violins give the SEOBNRv4 results for GW170729 and GW170814. Here $\tilde{A}_\alpha := A_\alpha / (10^{-19} \text{ peV}^{2-\alpha})$. We have let the much less constraining posteriors extend off the edges of the plots in order to show the more constraining posteriors in detail. The violin plots are scaled so that the maximum value of the posterior always has the same width, and these maximum values never occur off the plot.

than a simple SNR cut, for example, including information like the number of cycles of the signal in band, may be used to select which events will provide useful constraints.

Both here and in Sec. VI we report results on the parametrized deviations in the PN regime using two waveform models, IMRPHENOMPv2 and SEOBNRv4. There is a subtle difference between the ways deviations from GR are introduced and parametrized in the two models. With IMRPHENOMPv2, we directly constrain $\delta\hat{\varphi}_i$, which represent fractional deviations in the nonspinning portion of the $(i/2)$ PN phase coefficients. The SEOBNRv4 analysis instead uses a parametrization that also applies the fractional deviations to spin contributions, as described in [8]. The results are then mapped *post hoc* from this native parametrization to posteriors on $\delta\hat{\varphi}_i$, shown in Figs. 3 and 8 (black solid lines).

In the SEOBNRv4 analysis at 3.5 PN, the native (spin-inclusive) posteriors contain tails that extend to the edge of the prior range. This is due to a zero crossing of the 3.5 PN term in the (η, a_1, a_2) parameter space, which makes the corresponding relative deviation ill defined. After the *post hoc* mapping to posteriors on $\delta\hat{\varphi}_7$, no tails appear and we find good agreement with the IMRPHENOMPv2 analysis, as expected. By varying the prior range, we estimate a

systematic uncertainty of at most a few percent on the quoted 90% bounds due to the truncation of tails.

4. Parametrized tests of gravitational-wave propagation

Posteriors on A_α for individual events are shown in Fig. 10, with data for positive and negative A_α combined into one violin plot. We provide results for all events with the IMRPHENOMPv2 waveform model and also show results of the analysis with the SEOBNRv4 waveform model for GW170729 and GW170814. In Table VI we compare the 90% bounds on A_α and GR quantiles obtained with IMRPHENOMPv2 and SEOBNRv4 for GW170729 and GW170814. We focus on these two events because the GR quantiles obtained with IMRPHENOMPv2 lie in the tails of the distributions, and we find that this remains true for most α values in the analysis with SEOBNRv4. For GW170729 and $\alpha \in \{0, 0.5, 1\}$, the GR quantiles obtained using the two waveforms differ by factors of ~ 2 ; the two waveforms give values that are in much closer agreement for the other cases.

Additionally, for the GW151012 event and certain α values, a technical issue with our computation of the likelihood meant that specific points with relatively large

TABLE VI. 90% credible level upper bounds on the absolute value of the modified dispersion relation parameter A_α , as well as the GR quantiles Q_{GR} for IMRPHENOMPv2 (P) and SEOBNRV4 (S) runs. The $<$ and $>$ labels denote the bounds for $A_\alpha < 0$ and > 0 , respectively, with the given scalings and $\bar{A}_\alpha := A_\alpha/eV^{2-\alpha}$.

| Quantity | GW170729 | | | | | | GW170814 | | | | | |
|--------------------------------|----------|------|------|------|--------------|----|----------|-----|-----|-----|--------------|-----|
| | $<$ | | $>$ | | Q_{GR} [%] | | $<$ | | $>$ | | Q_{GR} [%] | |
| | P | S | P | S | P | S | P | S | P | S | P | S |
| \bar{A}_0 [10^{-44}] | 0.29 | 0.67 | 0.64 | 0.67 | 17 | 39 | 4.0 | 2.7 | 1.1 | 1.4 | 94 | 87 |
| $\bar{A}_{0.5}$ [10^{-38}] | 0.93 | 0.86 | 1.1 | 1.8 | 26 | 16 | 5.2 | 7.6 | 1.8 | 1.8 | 92 | 92 |
| \bar{A}_1 [10^{-32}] | 2.1 | 4.6 | 4.5 | 4.2 | 16 | 26 | 15 | 12 | 5.2 | 4.0 | 93 | 95 |
| $\bar{A}_{1.5}$ [10^{-25}] | 0.79 | 0.74 | 1.5 | 1.2 | 18 | 17 | 3.0 | 2.8 | 1.3 | 1.0 | 96 | 94 |
| $\bar{A}_{2.5}$ [10^{-13}] | 4.2 | 4.7 | 1.4 | 1.6 | 94 | 92 | 1.3 | 1.2 | 3.9 | 4.7 | 5.7 | 5.1 |
| \bar{A}_3 [10^{-8}] | 36 | 30 | 8.6 | 16 | 96 | 92 | 7.4 | 8.3 | 25 | 36 | 6.2 | 6.4 |
| $\bar{A}_{3.5}$ [10^{-2}] | 26 | 32 | 8.9 | 12 | 94 | 94 | 5.4 | 5.9 | 29 | 17 | 7.5 | 8.5 |
| \bar{A}_4 [10^4] | 43 | 47 | 7.1 | 9.1 | 95 | 95 | 4.2 | 4.7 | 13 | 20 | 9.6 | 11 |

values of A_α had to be manually removed from the posterior distribution. In particular, for computational efficiency, the likelihood is calculated on as short a segment of data as is practical, with duration set by the longest waveform to be sampled. Large values of A_α yield highly dispersed waveforms that are pushed beyond the confines of the segment we use, causing the waveform templates to wrap around the boundaries. This invalidates the assumptions underlying our likelihood computation and causes an artificial enhancement of the SNR as reported by the analysis. As expected, recomputing the SNRs for these points on a segment that properly fits the waveform results in smaller values that are consistent with noise. Therefore, we exclude from our analysis parameter values yielding waveforms that would not be contained by the data segment used, which is equivalent to using a stricter prior on A_α . Failure to do this may result in the appearance of outliers with spuriously high likelihood for large values of A_α , as we have seen in our own analysis.

- [1] C. M. Will, The confrontation between general relativity and experiment, *Living Rev. Relativity* **17**, 4 (2014).
- [2] J. Aasi *et al.* (LIGO Scientific Collaboration), Advanced LIGO, *Classical Quantum Gravity* **32**, 074001 (2015).
- [3] F. Acernese *et al.* (Virgo Collaboration), Advanced Virgo: A second-generation interferometric gravitational wave detector, *Classical Quantum Gravity* **32**, 024001 (2015).
- [4] B. P. Abbott *et al.* (LIGO Scientific and Virgo Collaborations), Tests of General Relativity with GW150914, *Phys. Rev. Lett.* **116**, 221101 (2016); Erratum, *Phys. Rev. Lett.* **121**, 129902(E) (2018).
- [5] B. P. Abbott *et al.* (LIGO Scientific and Virgo Collaborations), Binary Black Hole Mergers in the first Advanced LIGO Observing Run, *Phys. Rev. X* **6**, 041015 (2016); Erratum, *Phys. Rev. X* **8**, 039903(E) (2018).
- [6] B. P. Abbott *et al.* (LIGO Scientific and Virgo Collaborations), GW170104: Observation of a 50-Solar-Mass Binary Black Hole Coalescence at Redshift 0.2, *Phys. Rev. Lett.* **118**, 221101 (2017); Erratum, *Phys. Rev. Lett.* **121**, 129901(E) (2018).
- [7] B. P. Abbott *et al.* (LIGO Scientific and Virgo Collaborations), GW170814: A Three-Detector Observation of Gravitational Waves from a Binary Black Hole Coalescence, *Phys. Rev. Lett.* **119**, 141101 (2017).
- [8] B. P. Abbott *et al.* (LIGO Scientific and Virgo Collaborations), Tests of General Relativity with GW170817, *Phys. Rev. Lett.* **123**, 011102 (2019).
- [9] LIGO Scientific and Virgo Collaborations, GWTC-1, <https://doi.org/10.7935/82H3-HH23> (2018).
- [10] B. P. Abbott *et al.* (LIGO Scientific and Virgo Collaborations), Observation of Gravitational Waves from a Binary Black Hole Merger, *Phys. Rev. Lett.* **116**, 061102 (2016).
- [11] B. P. Abbott *et al.* (LIGO Scientific and Virgo Collaborations), GW150914: First results from the search for binary black hole coalescence with Advanced LIGO, *Phys. Rev. D* **93**, 122003 (2016).
- [12] B. P. Abbott *et al.* (LIGO Scientific and Virgo Collaborations), GW151226: Observation of Gravitational Waves from a 22-Solar-Mass Binary Black Hole Coalescence, *Phys. Rev. Lett.* **116**, 241103 (2016).
- [13] B. P. Abbott *et al.* (LIGO Scientific and Virgo Collaborations), GW170608: Observation of a 19 solar-mass binary black hole coalescence, *Astrophys. J. Lett.* **851**, L35 (2017).
- [14] B. P. Abbott *et al.* (LIGO Scientific and Virgo Collaborations), GWTC-1: A Gravitational-Wave Transient Catalog of Compact Binary Mergers Observed by LIGO and Virgo during the First and Second Observing Runs, *Phys. Rev. X* **9**, 031040 (2019).
- [15] B. P. Abbott *et al.* (LIGO Scientific and Virgo Collaborations), Observing gravitational-wave transient GW150914 with minimal assumptions, *Phys. Rev. D* **93**, 122004 (2016).
- [16] M. Vallisneri and N. Yunes, Stealth bias in gravitational-wave parameter estimation, *Phys. Rev. D* **87**, 102002 (2013).
- [17] S. Vitale and W. Del Pozzo, How serious can the stealth bias be in gravitational wave parameter estimation?, *Phys. Rev. D* **89**, 022002 (2014).
- [18] M. Okounkova, L. C. Stein, M. A. Scheel, and D. A. Hemberger, Numerical binary black hole mergers in

- dynamical Chern-Simons gravity: Scalar field, *Phys. Rev. D* **96**, 044020 (2017).
- [19] H. Witek, L. Gualtieri, P. Pani, and T.P. Sotiriou, Black holes and binary mergers in scalar Gauss-Bonnet gravity: Scalar field dynamics, *Phys. Rev. D* **99**, 064035 (2019).
- [20] M. Okounkova, L. C. Stein, M. A. Scheel, and S. A. Teukolsky, Numerical binary black hole collisions in dynamical Chern-Simons gravity, [arXiv:1906.08789](https://arxiv.org/abs/1906.08789).
- [21] A. Bohé *et al.*, Improved effective-one-body model of spinning, nonprecessing binary black holes for the era of gravitational-wave astrophysics with advanced detectors, *Phys. Rev. D* **95**, 044028 (2017).
- [22] S. Khan, S. Husa, M. Hannam, F. Ohme, M. Pürrer, X. Jiménez Forteza, and A. Bohé, Frequency-domain gravitational waves from nonprecessing black hole binaries. II. A phenomenological model for the advanced detector era, *Phys. Rev. D* **93**, 044007 (2016).
- [23] J. Blackman, S. E. Field, M. A. Scheel, C. R. Galley, D. A. Hemberger, P. Schmidt, and R. Smith, A surrogate model of gravitational waveforms from numerical relativity simulations of precessing binary black hole mergers, *Phys. Rev. D* **95**, 104023 (2017).
- [24] S. Khan, K. Chatziioannou, M. Hannam, and F. Ohme, Phenomenological model for the gravitational-wave signal from precessing binary black holes with two-spin effects, *Phys. Rev. D* **100**, 024059 (2019).
- [25] B. P. Abbott *et al.* (LIGO Scientific and Virgo Collaborations), Effects of waveform model systematics on the interpretation of GW150914, *Classical Quantum Gravity* **34**, 104002 (2017).
- [26] LIGO Scientific and Virgo Collaborations, Data release for testing GR with GWTC-1, <https://dcc.ligo.org/LIGO-P1900087/public> (2019).
- [27] LIGO Scientific and Virgo Collaborations, Gravitational Wave Open Science Center, <https://www.gw-openscience.org> (2018).
- [28] S. Karki *et al.*, The Advanced LIGO photon calibrators, *Rev. Sci. Instrum.* **87**, 114503 (2016).
- [29] C. Cahillane *et al.*, Calibration uncertainty for Advanced LIGO's first and second observing runs, *Phys. Rev. D* **96**, 102001 (2017).
- [30] A. Viets *et al.*, Reconstructing the calibrated strain signal in the Advanced LIGO detectors, *Classical Quantum Gravity* **35**, 095015 (2018).
- [31] D. Estevez *et al.*, V1O2Repro2A h(t) reprocessing for Virgo O2 data, Virgo Technical Report No. VIR-0362A-18, 2018, <https://tds.virgo-gw.eu/ql/?c=13254>.
- [32] F. Acernese *et al.* (Virgo Collaboration), Calibration of advanced Virgo and reconstruction of the gravitational wave signal $h(t)$ during the observing Run O2, *Classical Quantum Gravity* **35**, 205004 (2018).
- [33] W. M. Farr, B. Farr, and T. Littenberg, Modelling calibration errors in CBC waveforms, LIGO Technical Report No. LIGO-T1400682, 2015, <https://dcc.ligo.org/LIGO-T1400682/public>.
- [34] J. Veitch *et al.*, Robust parameter estimation for compact binaries with ground-based gravitational-wave observations using the LALInference software library, *Phys. Rev. D* **91**, 042003 (2015).
- [35] B. P. Abbott *et al.* (LIGO Scientific and Virgo Collaborations), Properties of the Binary Neutron Star Merger GW170817, *Phys. Rev. X* **9**, 011001 (2019).
- [36] B. P. Abbott *et al.* (LIGO Scientific and Virgo Collaborations), GW170817: Observation of Gravitational Waves from a Binary Neutron Star Inspiral, *Phys. Rev. Lett.* **119**, 161101 (2017).
- [37] J. C. Driggers *et al.* (LIGO Scientific Collaboration Instrument Science Authors), Improving astrophysical parameter estimation via offline noise subtraction for Advanced LIGO, *Phys. Rev. D* **99**, 042001 (2019).
- [38] D. Davis, T. J. Massinger, A. P. Lundgren, J. C. Driggers, A. L. Urban, and L. K. Nuttall, Improving the sensitivity of advanced LIGO using noise subtraction, *Classical Quantum Gravity* **36**, 055011 (2019).
- [39] S. Klimentenko, I. Yakushin, A. Mercer, and G. Mitselmakher, Coherent method for detection of gravitational wave bursts, *Classical Quantum Gravity* **25**, 114029 (2008).
- [40] S. Klimentenko *et al.*, Method for detection and reconstruction of gravitational wave transients with networks of advanced detectors, *Phys. Rev. D* **93**, 042004 (2016).
- [41] A. Ghosh, N. K. Johnson-McDaniel, A. Ghosh, C. K. Mishra, P. Ajith, W. Del Pozzo, C. P. L. Berry, A. B. Nielsen, and L. London, Testing general relativity using gravitational wave signals from the inspiral, merger and ringdown of binary black holes, *Classical Quantum Gravity* **35**, 014002 (2018).
- [42] M. Agathos, W. Del Pozzo, T. G. F. Li, C. Van Den Broeck, J. Veitch, and S. Vitale, TIGER: A data analysis pipeline for testing the strong-field dynamics of general relativity with gravitational wave signals from coalescing compact binaries, *Phys. Rev. D* **89**, 082001 (2014).
- [43] A. Zimmerman, C.-J. Haster, and K. Chatziioannou, On combining information from multiple gravitational wave sources, *Phys. Rev. D* **99**, 124044 (2019).
- [44] M. Isi, K. Chatziioannou, and W. M. Farr, Hierarchical Test of General Relativity with Gravitational Waves, *Phys. Rev. Lett.* **123**, 121101 (2019).
- [45] A. H. Nitz *et al.*, PyCBC software, <https://github.com/ligo-cbc/pycbc> (2018).
- [46] T. Dal Canton *et al.*, Implementing a search for aligned-spin neutron star-black hole systems with advanced ground based gravitational wave detectors, *Phys. Rev. D* **90**, 082004 (2014).
- [47] S. A. Usman *et al.*, The PyCBC search for gravitational waves from compact binary coalescence, *Classical Quantum Gravity* **33**, 215004 (2016).
- [48] S. Sachdev *et al.*, The GstLAL search analysis methods for compact binary mergers in Advanced LIGO's second and advanced Virgo's first observing runs, [arXiv:1901.08580](https://arxiv.org/abs/1901.08580).
- [49] C. Messick *et al.*, Analysis framework for the prompt discovery of compact binary mergers in gravitational-wave data, *Phys. Rev. D* **95**, 042001 (2017).
- [50] P. C. Peters and J. Mathews, Gravitational radiation from point masses in a Keplerian orbit, *Phys. Rev.* **131**, 435 (1963).
- [51] P. C. Peters, Gravitational radiation and the motion of two point masses, *Phys. Rev.* **136**, B1224 (1964).

- [52] T. Hinderer and S. Babak, Foundations of an effective-one-body model for coalescing binaries on eccentric orbits, *Phys. Rev. D* **96**, 104048 (2017).
- [53] Z. Cao and W.-B. Han, Waveform model for an eccentric binary black hole based on the effective-one-body-numerical-relativity formalism, *Phys. Rev. D* **96**, 044028 (2017).
- [54] I. Hinder, L. E. Kidder, and H. P. Pfeiffer, Eccentric binary black hole inspiral-merger-ringdown gravitational waveform model from numerical relativity and post-Newtonian theory, *Phys. Rev. D* **98**, 044015 (2018).
- [55] E. A. Huerta *et al.*, Eccentric, nonspinning, inspiral, Gaussian-process merger approximant for the detection and characterization of eccentric binary black hole mergers, *Phys. Rev. D* **97**, 024031 (2018).
- [56] A. Klein, Y. Boetzel, A. Gopakumar, P. Jetzer, and L. de Vittori, Fourier domain gravitational waveforms for precessing eccentric binaries, *Phys. Rev. D* **98**, 104043 (2018).
- [57] B. Moore, T. Robson, N. Loutrel, and N. Yunes, Towards a Fourier domain waveform for nonspinning binaries with arbitrary eccentricity, *Classical Quantum Gravity* **35**, 235006 (2018).
- [58] B. Moore and N. Yunes, A 3PN Fourier domain waveform for nonspinning binaries with moderate eccentricity, *Classical Quantum Gravity* **36**, 185003 (2019).
- [59] S. Tiwari, G. Achamveedu, M. Haney, and P. Hemantakumar, Ready-to-use Fourier domain templates for compact binaries inspiraling along moderately eccentric orbits, *Phys. Rev. D* **99**, 124008 (2019).
- [60] J. Samsing, Eccentric black hole mergers forming in globular clusters, *Phys. Rev. D* **97**, 103014 (2018).
- [61] C. L. Rodriguez, P. Amaro-Seoane, S. Chatterjee, and F. A. Rasio, post-Newtonian Dynamics in Dense Star Clusters: Highly-Eccentric, Highly-Spinning, and Repeated Binary Black Hole Mergers, *Phys. Rev. Lett.* **120**, 151101 (2018).
- [62] M. Zevin, J. Samsing, C. Rodriguez, C.-J. Haster, and E. Ramirez-Ruiz, Eccentric black hole mergers in dense star clusters: The role of binary-binary encounters, *Astrophys. J.* **871**, 91 (2019).
- [63] C. L. Rodriguez, P. Amaro-Seoane, S. Chatterjee, K. Kremer, F. A. Rasio, J. Samsing, C. S. Ye, and M. Zevin, post-Newtonian dynamics in dense star clusters: Formation, masses, and merger rates of highly-eccentric black hole binaries, *Phys. Rev. D* **98**, 123005 (2018).
- [64] S. Husa, S. Khan, M. Hannam, M. Pürrer, F. Ohme, X. J. Forteza, and A. Bohé, Frequency-domain gravitational waves from nonprecessing black hole binaries. I. New numerical waveforms and anatomy of the signal, *Phys. Rev. D* **93**, 044006 (2016).
- [65] M. Hannam, P. Schmidt, A. Bohé, L. Haegel, S. Husa, F. Ohme, G. Pratten, and M. Pürrer, Simple Model of Complete Precessing black hole-Binary Gravitational Waveforms, *Phys. Rev. Lett.* **113**, 151101 (2014).
- [66] A. Taracchini *et al.*, Effective-one-body model for black hole binaries with generic mass ratios and spins, *Phys. Rev. D* **89**, 061502 (2014).
- [67] S. Babak, A. Taracchini, and A. Buonanno, Validating the effective-one-body model of spinning, precessing binary black holes against numerical relativity, *Phys. Rev. D* **95**, 024010 (2017).
- [68] J. Blackman, S. E. Field, M. A. Scheel, C. R. Galley, C. D. Ott, M. Boyle, L. E. Kidder, H. P. Pfeiffer, and B. Szilágyi, Numerical relativity waveform surrogate model for generically precessing binary black hole mergers, *Phys. Rev. D* **96**, 024058 (2017).
- [69] V. Varma, S. E. Field, M. A. Scheel, J. Blackman, D. Gerosa, L. C. Stein, L. E. Kidder, and H. P. Pfeiffer, Surrogate models for precessing binary black hole simulations with unequal masses, *Phys. Rev. Research* **1**, 033015 (2019).
- [70] I. Kamaretsos, M. Hannam, S. Husa, and B. S. Sathyaprakash, black hole hair loss: Learning about binary progenitors from ringdown signals, *Phys. Rev. D* **85**, 024018 (2012).
- [71] L. London, D. Shoemaker, and J. Healy, Modeling ringdown: Beyond the fundamental quasinormal modes, *Phys. Rev. D* **90**, 124032 (2014); Erratum, *Phys. Rev. D* **94**, 069902(E) (2016).
- [72] L. London, S. Khan, E. Fauchon-Jones, C. García, M. Hannam, S. Husa, X. Jiménez-Forteza, C. Kalaghatgi, F. Ohme, and F. Pannarale, First Higher-Multipole Model of Gravitational Waves from Spinning and Coalescing black hole Binaries, *Phys. Rev. Lett.* **120**, 161102 (2018).
- [73] R. Cotesta, A. Buonanno, A. Bohé, A. Taracchini, I. Hinder, and S. Ossokine, Enriching the symphony of gravitational waves from binary black holes by tuning higher harmonics, *Phys. Rev. D* **98**, 084028 (2018).
- [74] V. Varma, S. E. Field, M. A. Scheel, J. Blackman, L. E. Kidder, and H. P. Pfeiffer, Surrogate model of hybridized numerical relativity binary black hole waveforms, *Phys. Rev. D* **99**, 064045 (2019).
- [75] V. Varma and P. Ajith, Effects of nonquadrupole modes in the detection and parameter estimation of black hole binaries with nonprecessing spins, *Phys. Rev. D* **96**, 124024 (2017).
- [76] P. T. H. Pang, J. C. Bustillo, Y. Wang, and T. G. F. Li, Potential observations of false deviations from general relativity in gravitational wave signals from binary black holes, *Phys. Rev. D* **98**, 024019 (2018).
- [77] LIGO Scientific and Virgo Collaborations, LALSuite software (2018), <https://doi.org/10.7935/GT1W-FZ16>.
- [78] N. J. Cornish and T. B. Littenberg, BayesWave: Bayesian inference for gravitational wave bursts and instrument glitches, *Classical Quantum Gravity* **32**, 135012 (2015).
- [79] T. B. Littenberg and N. J. Cornish, Bayesian inference for spectral estimation of gravitational wave detector noise, *Phys. Rev. D* **91**, 084034 (2015).
- [80] T. A. Apostolatos, Search templates for gravitational waves from precessing and inspiraling binaries, *Phys. Rev. D* **52**, 605 (1995).
- [81] R. A. Fisher, Questions and answers, *Am. Stat.* **2**, 30 (1948).
- [82] A. Ghosh *et al.*, Testing general relativity using golden black hole binaries, *Phys. Rev. D* **94**, 021101(R) (2016).
- [83] J. M. Bardeen, W. H. Press, and S. A. Teukolsky, Rotating black holes: Locally nonrotating frames, energy extraction, and scalar synchrotron radiation, *Astrophys. J.* **178**, 347 (1972).
- [84] J. Healy and C. O. Lousto, Remnant of binary black hole mergers: New simulations and peak luminosity studies, *Phys. Rev. D* **95**, 024037 (2017).

- [85] F. Hofmann, E. Barausse, and L. Rezzolla, The final spin from binary black holes in quasi-circular orbits, *Astrophys. J. Lett.* **825**, L19 (2016).
- [86] X. Jiménez-Forteza, D. Keitel, S. Husa, M. Hannam, S. Khan, and M. Pürrer, Hierarchical data-driven approach to fitting numerical relativity data for nonprecessing binary black holes with an application to final spin and radiated energy, *Phys. Rev. D* **95**, 064024 (2017).
- [87] N. K. Johnson-McDaniel *et al.*, Determining the final spin of a binary black hole system including in-plane spins: Method and checks of accuracy, LIGO Technical Report No. LIGO-T1600168, 2016, <https://dcc.ligo.org/LIGO-T1600168/public/main>.
- [88] L. Blanchet, T. Damour, B. R. Iyer, C. M. Will, and A. G. Wiseman, Gravitational-Radiation Damping of Compact Binary Systems to Second post-Newtonian Order, *Phys. Rev. Lett.* **74**, 3515 (1995).
- [89] L. Blanchet, T. Damour, G. Esposito-Farèse, and B. R. Iyer, Gravitational Radiation from Inspiralling Compact Binaries Completed at the Third post-Newtonian Order, *Phys. Rev. Lett.* **93**, 091101 (2004).
- [90] L. Blanchet, T. Damour, G. Esposito-Farèse, and B. R. Iyer, Dimensional regularization of the third post-Newtonian gravitational wave generation from two point masses, *Phys. Rev. D* **71**, 124004 (2005).
- [91] L. Blanchet, Gravitational radiation from post-Newtonian sources and inspiralling compact binaries, *Living Rev. Relativity* **17**, 2 (2014).
- [92] K. G. Arun, B. R. Iyer, M. S. S. Qusailah, and B. S. Sathyaprakash, Probing the nonlinear structure of general relativity with black hole binaries, *Phys. Rev. D* **74**, 024006 (2006).
- [93] K. G. Arun, B. R. Iyer, M. S. S. Qusailah, and B. S. Sathyaprakash, Testing post-Newtonian theory with gravitational wave observations, *Classical Quantum Gravity* **23**, L37 (2006).
- [94] C. K. Mishra, K. G. Arun, B. R. Iyer, and B. S. Sathyaprakash, Parametrized tests of post-Newtonian theory using Advanced LIGO and Einstein telescope, *Phys. Rev. D* **82**, 064010 (2010).
- [95] N. Yunes and F. Pretorius, Fundamental theoretical bias in gravitational wave astrophysics and the parametrized post-Einsteinian framework, *Phys. Rev. D* **80**, 122003 (2009).
- [96] T. G. F. Li, W. Del Pozzo, S. Vitale, C. Van Den Broeck, M. Agathos, J. Veitch, K. Grover, T. Sidery, R. Sturani, and A. Vecchio, Towards a generic test of the strong field dynamics of general relativity using compact binary coalescence, *Phys. Rev. D* **85**, 082003 (2012).
- [97] T. G. F. Li, W. Del Pozzo, S. Vitale, C. Van Den Broeck, M. Agathos, J. Veitch, K. Grover, T. Sidery, R. Sturani, and A. Vecchio, Towards a generic test of the strong field dynamics of general relativity using compact binary coalescence: Further investigations, *J. Phys. Conf. Ser.* **363**, 012028 (2012).
- [98] N. Cornish, L. Sampson, N. Yunes, and F. Pretorius, Gravitational wave tests of general relativity with the parametrized post-Einsteinian framework, *Phys. Rev. D* **84**, 062003 (2011).
- [99] L. Sampson, N. Cornish, and N. Yunes, Mismodeling in gravitational-wave astronomy: The trouble with templates, *Phys. Rev. D* **89**, 064037 (2014).
- [100] J. Meidam *et al.*, Parametrized tests of the strong-field dynamics of general relativity using gravitational wave signals from coalescing binary black holes: Fast likelihood calculations and sensitivity of the method, *Phys. Rev. D* **97**, 044033 (2018).
- [101] N. Yunes, K. Yagi, and F. Pretorius, Theoretical physics implications of the binary black hole mergers GW150914 and GW151226, *Phys. Rev. D* **94**, 084002 (2016).
- [102] K. Yagi, L. C. Stein, and N. Yunes, Challenging the presence of scalar charge and dipolar radiation in binary pulsars, *Phys. Rev. D* **93**, 024010 (2016).
- [103] K. Yagi and L. C. Stein, Black hole based tests of general relativity, *Classical Quantum Gravity* **33**, 054001 (2016).
- [104] E. Barausse, N. Yunes, and K. Chamberlain, Theory-Agnostic Constraints on black hole Dipole Radiation with Multiband Gravitational-Wave Astrophysics, *Phys. Rev. Lett.* **116**, 241104 (2016).
- [105] K. G. Arun, Generic bounds on dipolar gravitational radiation from inspiralling compact binaries, *Classical Quantum Gravity* **29**, 075011 (2012).
- [106] L. Sampson, N. Cornish, and N. Yunes, Gravitational wave tests of strong field general relativity with binary inspirals: Realistic injections and optimal model selection, *Phys. Rev. D* **87**, 102001 (2013).
- [107] M. Kramer *et al.*, Tests of general relativity from timing the double pulsar, *Science* **314**, 97 (2006).
- [108] N. Yunes and S. A. Hughes, Binary pulsar constraints on the parametrized post-Einsteinian framework, *Phys. Rev. D* **82**, 082002 (2010).
- [109] S. Mirshekari, N. Yunes, and C. M. Will, Constraining generic Lorentz violation and the speed of the graviton with gravitational waves, *Phys. Rev. D* **85**, 024041 (2012).
- [110] B. P. Abbott *et al.* (LIGO Scientific, Virgo, Fermi-GBM, and INTEGRAL Collaborations), Gravitational waves and Gamma-rays from a binary neutron star merger: GW170817 and GRB 170817A, *Astrophys. J. Lett.* **848**, L13 (2017).
- [111] C. M. Will, Bounding the mass of the graviton using gravitational wave observations of inspiralling compact binaries, *Phys. Rev. D* **57**, 2061 (1998).
- [112] G. Calcagni, Fractal Universe and Quantum Gravity, *Phys. Rev. Lett.* **104**, 251301 (2010).
- [113] G. Amelino-Camelia, Doubly special relativity, *Nature (London)* **418**, 34 (2002).
- [114] P. Hořava, Quantum gravity at a Lifshitz point, *Phys. Rev. D* **79**, 084008 (2009).
- [115] A. S. Sefiedgar, K. Nozari, and H. R. Sepangi, Modified dispersion relations in extra dimensions, *Phys. Lett. B* **696**, 119 (2011).
- [116] V. A. Kostelecký and M. Mewes, Testing local Lorentz invariance with gravitational waves, *Phys. Lett. B* **757**, 510 (2016).
- [117] P. A. R. Ade *et al.* (Planck Collaboration), Planck 2015 results. XIII. Cosmological parameters, *Astron. Astrophys.* **594**, A13 (2016).

- [118] N. Aghanim *et al.* (Planck Collaboration), Planck 2018 results. VI. Cosmological parameters, [arXiv: 1807.06209](https://arxiv.org/abs/1807.06209).
- [119] G. Amelino-Camelia, M. Arzano, Y. Ling, and G. Mandanici, black hole thermodynamics with modified dispersion relations and generalized uncertainty principles, *Classical Quantum Gravity* **23**, 2585 (2006).
- [120] G. Calcagni, Lorentz violations in multifractal space-times, *Eur. Phys. J. C* **77**, 291 (2017).
- [121] L. Bernus, O. Minazzoli, A. Fienga, M. Gastineau, J. Laskar, and P. Deram, Constraining the Mass of the Graviton with the Planetary Ephemeris INPOP, *Phys. Rev. Lett.*, **123**, 161103 (2019).
- [122] C. M. Will, Solar system vs. gravitational-wave bounds on the graviton mass, *Classical Quantum Gravity* **35**, 17LT01 (2018).
- [123] C. de Rham, J. T. Deskins, A. J. Tolley, and S.-Y. Zhou, Graviton mass bounds, *Rev. Mod. Phys.* **89**, 025004 (2017).
- [124] D. B. Rubin, The Bayesian bootstrap, *Ann. Stat.* **9**, 130 (1981).
- [125] D. M. Eardley, D. L. Lee, and A. P. Lightman, Gravitational-wave observations as a tool for testing relativistic gravity, *Phys. Rev. D* **8**, 3308 (1973).
- [126] K. Chatziioannou, N. Yunes, and N. Cornish, Model-independent test of general relativity: An extended post-Einsteinian framework with complete polarization content, *Phys. Rev. D* **86**, 022004 (2012); Erratum, *Phys. Rev. D* **95**, 129901(E) (2017).
- [127] M. Isi, M. Pitkin, and A. J. Weinstein, Probing dynamical gravity with the polarization of continuous gravitational waves, *Phys. Rev. D* **96**, 042001 (2017).
- [128] T. Callister, A. S. Biscoveanu, N. Christensen, M. Isi, A. Matas, O. Minazzoli, T. Regimbau, M. Sakellariadou, J. Tasson, and E. Thrane, Polarization-Based Tests of Gravity with the Stochastic Gravitational-Wave Background, *Phys. Rev. X* **7**, 041058 (2017).
- [129] M. Isi and A. J. Weinstein, Probing gravitational wave polarizations with signals from compact binary coalescences, LIGO Tech. Note No. LIGO-P1700276, 2017, <https://dcc.ligo.org/LIGO-P1700276/public>.
- [130] A. Blaut, Angular and frequency response of the gravitational wave interferometers in the metric theories of gravity, *Phys. Rev. D* **85**, 043005 (2012).
- [131] B. P. Abbott *et al.* (KAGRA, LIGO Scientific, and Virgo Collaborations), Prospects for observing and localizing gravitational-wave transients with Advanced LIGO, Advanced Virgo and KAGRA, *Living Rev. Relativity* **21**, 3 (2018).
- [132] B. P. Abbott *et al.* (LIGO Scientific and Virgo Collaborations), Directly comparing GW150914 with numerical solutions of Einstein's equations for binary black hole coalescence, *Phys. Rev. D* **94**, 064035 (2016).
- [133] J. Lange *et al.*, Parameter estimation method that directly compares gravitational wave observations to numerical relativity, *Phys. Rev. D* **96**, 104041 (2017).
- [134] G. Ashton *et al.*, Bilby: A user-friendly Bayesian inference library for gravitational-wave astronomy, *Astrophys. J. Suppl. Ser.* **241**, 27 (2019).

B. P. Abbott,¹ R. Abbott,¹ T. D. Abbott,² S. Abraham,³ F. Acernese,^{4,5} K. Ackley,⁶ C. Adams,⁷ R. X. Adhikari,¹ V. B. Adya,^{8,9} C. Affeldt,^{8,9} M. Agathos,¹⁰ K. Agatsuma,¹¹ N. Aggarwal,¹² O. D. Aguiar,¹³ L. Aiello,^{14,15} A. Ain,³ P. Ajith,¹⁶ G. Allen,¹⁷ A. Allocca,^{18,19} M. A. Aloy,²⁰ P. A. Altin,²¹ A. Amato,²² A. Ananyeva,¹ S. B. Anderson,¹ W. G. Anderson,²³ S. V. Angelova,²⁴ S. Antier,²⁵ S. Appert,¹ K. Arai,¹ M. C. Araya,¹ J. S. Areeda,²⁶ M. Arène,²⁷ N. Arnaud,^{25,28} K. G. Arun,²⁹ S. Ascenzi,^{30,31} G. Ashton,⁶ S. M. Aston,⁷ P. Astone,³² F. Aubin,³³ P. Aufmuth,⁹ K. AultONeal,³⁴ C. Austin,² V. Avendano,³⁵ A. Avila-Alvarez,²⁶ S. Babak,^{36,27} P. Bacon,²⁷ F. Badaracco,^{14,15} M. K. M. Bader,³⁷ S. Bae,³⁸ P. T. Baker,³⁹ F. Baldaccini,^{40,41} G. Ballardin,²⁸ S. W. Ballmer,⁴² S. Banagiri,⁴³ J. C. Barayoga,¹ S. E. Barclay,⁴⁴ B. C. Barish,¹ D. Barker,⁴⁵ K. Barkett,⁴⁶ S. Barnum,¹² F. Barone,^{4,5} B. Barr,⁴⁴ L. Barsotti,¹² M. Barsuglia,²⁷ D. Barta,⁴⁷ J. Bartlett,⁴⁵ I. Bartos,⁴⁸ R. Bassiri,⁴⁹ A. Basti,^{18,19} M. Bawaj,^{50,41} J. C. Bayley,⁴⁴ M. Bazzan,^{51,52} B. Bécsy,⁵³ M. Bejger,^{27,54} I. Belahcene,²⁵ A. S. Bell,⁴⁴ D. Beniwal,⁵⁵ B. K. Berger,⁴⁹ G. Bergmann,^{8,9} S. Bernuzzi,^{56,57} J. J. Bero,⁵⁸ C. P. L. Berry,⁵⁹ D. Bersanetti,⁶⁰ A. Bertolini,³⁷ J. Betzwieser,⁷ R. Bhandare,⁶¹ J. Bidler,²⁶ I. A. Bilenko,⁶² S. A. Bilgili,³⁹ G. Billingsley,¹ J. Birch,⁷ R. Birney,²⁴ O. Birnholtz,⁵⁸ S. Biscans,^{1,12} S. Biscoveanu,⁶ A. Bisht,⁹ M. Bitossi,^{28,19} M. A. Bizouard,²⁵ J. K. Blackburn,¹ C. D. Blair,⁷ D. G. Blair,⁶³ R. M. Blair,⁴⁵ S. Bloemen,⁶⁴ N. Bode,^{8,9} M. Boer,⁶⁵ Y. Boetzel,⁶⁶ G. Bogaert,⁶⁵ F. Bondu,⁶⁷ E. Bonilla,⁴⁹ R. Bonnand,³³ P. Booker,^{8,9} B. A. Boom,³⁷ C. D. Booth,⁶⁸ R. Bork,¹ V. Boschi,²⁸ S. Bose,^{69,3} K. Bossie,⁷ V. Bossilkov,⁶³ J. Bosveld,⁶³ Y. Bouffanais,²⁷ A. Bozzi,²⁸ C. Bradaschia,¹⁹ P. R. Brady,²³ A. Bramley,⁷ M. Branchesi,^{14,15} J. E. Brau,⁷⁰ M. Breschi,⁵⁶ T. Briant,⁷¹ J. H. Briggs,⁴⁴ F. Brighenti,^{72,73} A. Brillet,⁶⁵ M. Brinkmann,^{8,9} V. Brisson,^{25,†} R. Brito,³⁶ P. Brockill,²³ A. F. Brooks,¹ D. D. Brown,⁵⁵ S. Brunett,¹ A. Buikema,¹² T. Bulik,⁷⁴ H. J. Bulten,^{75,37} A. Buonanno,^{36,76} D. Buskulic,³³ M. J. Bustamante Rosell,⁷⁷ C. Buy,²⁷ R. L. Byer,⁴⁹ M. Cabero,^{8,9} L. Cadonati,⁷⁸ G. Cagnoli,^{22,79} C. Cahillane,¹ J. Calderón Bustillo,⁶ T. A. Callister,¹ E. Calloni,^{80,5} J. B. Camp,⁸¹ W. A. Campbell,⁶ M. Canepa,^{82,60} K. C. Cannon,⁸³ H. Cao,⁵⁵ J. Cao,⁸⁴ C. D. Capano,⁸ E. Capocasa,²⁷ F. Carbognani,²⁸ S. Caride,⁸⁵ M. F. Carney,⁵⁹ G. Carullo,¹⁸ J. Casanueva Diaz,¹⁹ C. Casentini,^{30,31} S. Caudill,³⁷ M. Cavaglia,⁸⁶ F. Cavalier,²⁵ R. Cavalieri,²⁸ G. Cella,¹⁹ P. Cerdá-Durán,²⁰ G. Cerretani,^{18,19} E. Cesarini,^{87,31} O. Chaibi,⁶⁵ K. Chakravarti,³ S. J. Chamberlin,⁸⁸ M. Chan,⁴⁴ S. Chao,⁸⁹

P. Charlton,⁹⁰ E. A. Chase,⁵⁹ E. Chassande-Mottin,²⁷ D. Chatterjee,²³ M. Chaturvedi,⁶¹ K. Chatziioannou,⁹¹
 B. D. Cheeseboro,³⁹ H. Y. Chen,⁹² X. Chen,⁶³ Y. Chen,⁴⁶ H.-P. Cheng,⁴⁸ C. K. Cheong,⁹³ H. Y. Chia,⁴⁸ A. Chincarini,⁶⁰
 A. Chiummo,²⁸ G. Cho,⁹⁴ H. S. Cho,⁹⁵ M. Cho,⁷⁶ N. Christensen,^{65,96} Q. Chu,⁶³ S. Chua,⁷¹ K. W. Chung,⁹³ S. Chung,⁶³
 G. Ciani,^{51,52} A. A. Ciobanu,⁵⁵ R. Ciolfi,^{97,98} F. Cipriano,⁶⁵ A. Cirone,^{82,60} F. Clara,⁴⁵ J. A. Clark,⁷⁸ P. Clearwater,⁹⁹
 F. Cleva,⁶⁵ C. Cocchieri,⁸⁶ E. Coccia,^{14,15} P.-F. Cohadon,⁷¹ D. Cohen,²⁵ R. Colgan,¹⁰⁰ M. Colleoni,¹⁰¹ C. G. Collette,¹⁰²
 C. Collins,¹¹ L. R. Cominsky,¹⁰³ M. Constanancio Jr.,¹³ L. Conti,⁵² S. J. Cooper,¹¹ P. Corban,⁷ T. R. Corbitt,²
 I. Cordero-Carrión,¹⁰⁴ K. R. Corley,¹⁰⁰ N. Cornish,⁵³ A. Corsi,⁸⁵ S. Cortese,²⁸ C. A. Costa,¹³ R. Cotesta,³⁶ M. W. Coughlin,¹
 S. B. Coughlin,^{68,59} J.-P. Coulon,⁶⁵ S. T. Countryman,¹⁰⁰ P. Couvares,¹ P. B. Covas,¹⁰¹ E. E. Cowan,⁷⁸ D. M. Coward,⁶³
 M. J. Cowart,⁷ D. C. Coyne,¹ R. Coyne,¹⁰⁵ J. D. E. Creighton,²³ T. D. Creighton,¹⁰⁶ J. Cripe,² M. Croquette,⁷¹
 S. G. Crowder,¹⁰⁷ T. J. Cullen,² A. Cumming,⁴⁴ L. Cunningham,⁴⁴ E. Cuoco,²⁸ T. Dal Canton,⁸¹ G. Dálya,¹⁰⁸
 S. L. Danilishin,^{8,9} S. D'Antonio,³¹ K. Danzmann,^{9,8} A. Dasgupta,¹⁰⁹ C. F. Da Silva Costa,⁴⁸ L. E. H. Datrier,⁴⁴ V. Dattilo,²⁸
 I. Dave,⁶¹ M. Davier,²⁵ D. Davis,⁴² E. J. Daw,¹¹⁰ D. DeBra,⁴⁹ M. Deenadayalan,³ J. Degallaix,²² M. De Laurentis,^{80,5}
 S. Deléglise,⁷¹ W. Del Pozzo,^{18,19} L. M. DeMarchi,⁵⁹ N. Demos,¹² T. Dent,^{8,9,111} R. De Pietri,^{112,57} J. Derby,²⁶ R. De Rosa,^{80,5}
 C. De Rossi,^{22,28} R. DeSalvo,¹¹³ O. de Varona,^{8,9} S. Dhurandhar,³ M. C. Díaz,¹⁰⁶ T. Dietrich,³⁷ L. Di Fiore,⁵
 M. Di Giovanni,^{114,98} T. Di Girolamo,^{80,5} A. Di Lieto,^{18,19} B. Ding,¹⁰² S. Di Pace,^{115,32} I. Di Palma,^{115,32} F. Di Renzo,^{18,19}
 A. Dmitriev,¹¹ Z. Doctor,⁹² F. Donovan,¹² K. L. Dooley,^{68,86} S. Doravari,^{8,9} I. Dorrington,⁶⁸ T. P. Downes,²³ M. Drago,^{14,15}
 J. C. Driggers,⁴⁵ Z. Du,⁸⁴ J.-G. Ducoin,²⁵ P. Dupej,⁴⁴ S. E. Dwyer,⁴⁵ P. J. Easter,⁶ T. B. Edo,¹¹⁰ M. C. Edwards,⁹⁶ A. Effler,⁷
 P. Ehrens,¹ J. Eichholz,¹ S. S. Eikenberry,⁴⁸ M. Eisenmann,³³ R. A. Eisenstein,¹² R. C. Essick,⁹² H. Estelles,¹⁰¹ D. Estevez,³³
 Z. B. Etienne,³⁹ T. Etzel,¹ M. Evans,¹² T. M. Evans,⁷ V. Fafone,^{30,31,14} H. Fair,⁴² S. Fairhurst,⁶⁸ X. Fan,⁸⁴ S. Farinon,⁶⁰
 B. Farr,⁷⁰ W. M. Farr,¹¹ E. J. Fauchon-Jones,⁶⁸ M. Favata,³⁵ M. Fays,¹¹⁰ M. Fazio,¹¹⁶ C. Fee,¹¹⁷ J. Feicht,¹ M. M. Fejer,⁴⁹
 F. Feng,²⁷ A. Fernandez-Galiana,¹² I. Ferrante,^{18,19} E. C. Ferreira,¹³ T. A. Ferreira,¹³ F. Ferrini,²⁸ F. Fidecaro,^{18,19} I. Fiori,²⁸
 D. Fiorucci,²⁷ M. Fishbach,⁹² R. P. Fisher,^{42,118} J. M. Fishner,¹² M. Fitz-Axen,⁴³ R. Flaminio,^{33,119} M. Fletcher,⁴⁴ E. Flynn,²⁶
 H. Fong,⁹¹ J. A. Font,^{20,120} P. W. F. Forsyth,²¹ J.-D. Fournier,⁶⁵ S. Frasca,^{115,32} F. Frasconi,¹⁹ Z. Frei,¹⁰⁸ A. Freise,¹¹ R. Frey,⁷⁰
 V. Frey,²⁵ P. Fritschel,¹² V. V. Frolov,⁷ P. Fulda,⁴⁸ M. Fyffe,⁷ H. A. Gabbard,⁴⁴ B. U. Gadre,³ S. M. Gaebel,¹¹ J. R. Gair,¹²¹
 L. Gammaitoni,⁴⁰ M. R. Ganija,⁵⁵ S. G. Gaonkar,³ A. Garcia,²⁶ C. García-Quirós,¹⁰¹ F. Garufi,^{80,5} B. Gateley,⁴⁵ S. Gaudio,³⁴
 G. Gaur,¹²² V. Gayathri,¹²³ G. Gemme,⁶⁰ E. Genin,²⁸ A. Gennai,¹⁹ D. George,¹⁷ J. George,⁶¹ L. Gergely,¹²⁴ V. Germain,³³
 S. Ghonge,⁷⁸ Abhirup Ghosh,¹⁶ Archisman Ghosh,³⁷ S. Ghosh,²³ B. Giacomazzo,^{114,98} J. A. Giaime,^{2,7} K. D. Giardino,⁷
 A. Giazotto,^{19,†} K. Gill,³⁴ G. Giordano,^{4,5} L. Glover,¹¹³ P. Godwin,⁸⁸ E. Goetz,⁴⁵ R. Goetz,⁴⁸ B. Goncharov,⁶ G. González,²
 J. M. Gonzalez Castro,^{18,19} A. Gopakumar,¹²⁵ M. L. Gorodetsky,⁶² S. E. Gossan,¹ M. Gosselin,²⁸ R. Gouaty,³³ A. Grado,^{126,5}
 C. Graef,⁴⁴ M. Granata,²² A. Grant,⁴⁴ S. Gras,¹² P. Grassia,¹ C. Gray,⁴⁵ R. Gray,⁴⁴ G. Greco,^{72,73} A. C. Green,^{11,48} R. Green,⁶⁸
 E. M. Gretarsson,³⁴ P. Groot,⁶⁴ H. Grote,⁶⁸ S. Grunewald,³⁶ P. Gruning,²⁵ G. M. Guidi,^{72,73} H. K. Gulati,¹⁰⁹ Y. Guo,³⁷
 A. Gupta,⁸⁸ M. K. Gupta,¹⁰⁹ E. K. Gustafson,¹ R. Gustafson,¹²⁷ L. Haegel,¹⁰¹ O. Halim,^{15,14} B. R. Hall,⁶⁹ E. D. Hall,¹²
 E. Z. Hamilton,⁶⁸ G. Hammond,⁴⁴ M. Haney,⁶⁶ M. M. Hanke,^{8,9} J. Hanks,⁴⁵ C. Hanna,⁸⁸ M. D. Hannam,⁶⁸
 O. A. Hannuksela,⁹³ J. Hanson,⁷ T. Hardwick,² K. Haris,¹⁶ J. Harms,^{14,15} G. M. Harry,¹²⁸ I. W. Harry,³⁶ C.-J. Haster,⁹¹
 K. Haughian,⁴⁴ F. J. Hayes,⁴⁴ J. Healy,⁵⁸ A. Heidmann,⁷¹ M. C. Heintze,⁷ H. Heitmann,⁶⁵ P. Hello,²⁵ G. Hemming,²⁸
 M. Hendry,⁴⁴ I. S. Heng,⁴⁴ J. Hennig,^{8,9} A. W. Heptonstall,¹ Francisco Hernandez Vivanco,⁶ M. Heurs,^{8,9} S. Hild,⁴⁴
 T. Hinderer,^{129,37,130} D. Hoak,²⁸ S. Hochheim,^{8,9} D. Hofman,²² A. M. Holgado,¹⁷ N. A. Holland,²¹ K. Holt,⁷ D. E. Holz,⁹²
 P. Hopkins,⁶⁸ C. Horst,²³ J. Hough,⁴⁴ E. J. Howell,⁶³ C. G. Hoy,⁶⁸ A. Hreibi,⁶⁵ E. A. Huerta,¹⁷ D. Huet,²⁵ B. Hughey,³⁴
 M. Hulko,¹ S. Husa,¹⁰¹ S. H. Huttner,⁴⁴ T. Huynh-Dinh,⁷ B. Idzkowski,⁷⁴ A. Iess,^{30,31} C. Ingram,⁵⁵ R. Inta,⁸⁵ G. Intini,^{115,32}
 B. Irwin,¹¹⁷ H. N. Isa,⁴⁴ J.-M. Isac,⁷¹ M. Isi,¹ B. R. Iyer,¹⁶ K. Izumi,⁴⁵ T. Jacqmin,⁷¹ S. J. Jadhav,¹³¹ K. Jani,⁷⁸
 N. N. Janthapur,¹³¹ P. Jaranowski,¹³² A. C. Jenkins,¹³³ J. Jiang,⁴⁸ D. S. Johnson,¹⁷ N. K. Johnson-McDaniel,¹⁰ A. W. Jones,¹¹
 D. I. Jones,¹³⁴ R. Jones,⁴⁴ R. J. G. Jonker,³⁷ L. Ju,⁶³ J. Junker,^{8,9} C. V. Kalaghatgi,⁶⁸ V. Kalogera,⁵⁹ B. Kamai,¹
 S. Kandhasamy,⁸⁶ G. Kang,³⁸ J. B. Kanner,¹ S. J. Kapadia,²³ S. Karki,⁷⁰ K. S. Karvinen,^{8,9} R. Kashyap,¹⁶ M. Kasprzack,¹
 S. Katsanevas,²⁸ E. Katsavounidis,¹² W. Katzman,⁷ S. Kaufer,⁹ K. Kawabe,⁴⁵ N. V. Keerthana,³ F. Kéfélian,⁶⁵ D. Keitel,⁴⁴
 R. Kennedy,¹¹⁰ J. S. Key,¹³⁵ F. Y. Khalili,⁶² H. Khan,²⁶ I. Khan,^{14,31} S. Khan,^{8,9} Z. Khan,¹⁰⁹ E. A. Khazanov,¹³⁶
 M. Khursheed,⁶¹ N. Kijbunchoo,²¹ Chunglee Kim,¹³⁷ J. C. Kim,¹³⁸ K. Kim,⁹³ W. Kim,⁵⁵ W. S. Kim,¹³⁹ Y.-M. Kim,¹⁴⁰
 C. Kimball,⁵⁹ E. J. King,⁵⁵ P. J. King,⁴⁵ M. Kinley-Hanlon,¹²⁸ R. Kirchhoff,^{8,9} J. S. Kissel,⁴⁵ L. Kleybolte,¹⁴¹ J. H. Klika,²³
 S. Klimenko,⁴⁸ T. D. Knowles,³⁹ P. Koch,^{8,9} S. M. Koehlenbeck,^{8,9} G. Koekoek,^{37,142} S. Koley,³⁷ V. Kondrashov,¹
 A. Kontos,¹² N. Koper,^{8,9} M. Korobko,¹⁴¹ W. Z. Korth,¹ I. Kowalska,⁷⁴ D. B. Kozak,¹ V. Kringel,^{8,9} N. Krishnendu,²⁹

A. Królak,^{143,144} G. Kuehn,^{8,9} A. Kumar,¹³¹ P. Kumar,¹⁴⁵ R. Kumar,¹⁰⁹ S. Kumar,¹⁶ L. Kuo,⁸⁹ A. Kutynia,¹⁴³ S. Kwang,²³ B. D. Lackey,³⁶ K. H. Lai,⁹³ T. L. Lam,⁹³ M. Landry,⁴⁵ B. B. Lane,¹² R. N. Lang,¹⁴⁶ J. Lange,⁵⁸ B. Lantz,⁴⁹ R. K. Lanza,¹² A. Lartaux-Vollard,²⁵ P. D. Lasky,⁶ M. Laxen,⁷ A. Lazzarini,¹ C. Lazzaro,⁵² P. Leaci,^{115,32} S. Leavey,^{8,9} Y. K. Lecoeuche,⁴⁵ C. H. Lee,⁹⁵ H. K. Lee,¹⁴⁷ H. M. Lee,¹⁴⁸ H. W. Lee,¹³⁸ J. Lee,⁹⁴ K. Lee,⁴⁴ J. Lehmann,^{8,9} A. Lenon,³⁹ N. Leroy,²⁵ N. Letendre,³³ Y. Levin,^{6,100} J. Li,⁸⁴ K. J. L. Li,⁹³ T. G. F. Li,⁹³ X. Li,⁴⁶ F. Lin,⁶ F. Linde,³⁷ S. D. Linker,¹¹³ T. B. Littenberg,¹⁴⁹ J. Liu,⁶³ X. Liu,²³ R. K. L. Lo,^{93,1} N. A. Lockerbie,²⁴ L. T. London,⁶⁸ A. Longo,^{150,151} M. Lorenzini,^{14,15} V. Lorette,¹⁵² M. Lormand,⁷ G. Losurdo,¹⁹ J. D. Lough,^{8,9} C. O. Lousto,⁵⁸ G. Lovelace,²⁶ M. E. Lower,¹⁵³ H. Lück,^{9,8} D. Lumaca,^{30,31} A. P. Lundgren,¹⁵⁴ R. Lynch,¹² Y. Ma,⁴⁶ R. Macas,⁶⁸ S. Macfoy,²⁴ M. MacInnis,¹² D. M. Macleod,⁶⁸ A. Macquet,⁶⁵ F. Magaña-Sandoval,⁴² L. Magaña Zertuche,⁸⁶ R. M. Magee,⁸⁸ E. Majorana,³² I. Maksimovic,¹⁵² A. Malik,⁶¹ N. Man,⁶⁵ V. Mandic,⁴³ V. Mangano,⁴⁴ G. L. Mansell,^{45,12} M. Manske,^{23,21} M. Mantovani,²⁸ F. Marchesoni,^{50,41} F. Marion,³³ S. Márka,¹⁰⁰ Z. Márka,¹⁰⁰ C. Markakis,^{10,17} A. S. Markosyan,⁴⁹ A. Markowitz,¹ E. Maros,¹ A. Marquina,¹⁰⁴ S. Marsat,³⁶ F. Martelli,^{72,73} I. W. Martin,⁴⁴ R. M. Martin,³⁵ D. V. Martynov,¹¹ K. Mason,¹² E. Massera,¹¹⁰ A. Masserot,³³ T. J. Massinger,¹ M. Masso-Reid,⁴⁴ S. Mastrogiovanni,^{115,32} A. Matas,^{43,36} F. Matichard,^{1,12} L. Matone,¹⁰⁰ N. Mavalvala,¹² N. Mazumder,⁶⁹ J. J. McCann,⁶³ R. McCarthy,⁴⁵ D. E. McClelland,²¹ S. McCormick,⁷ L. McCuller,¹² S. C. McGuire,¹⁵⁵ J. McIver,¹ D. J. McManus,²¹ T. McRae,²¹ S. T. McWilliams,³⁹ D. Meacher,⁸⁸ G. D. Meadors,⁶ M. Mehmet,^{8,9} A. K. Mehta,¹⁶ J. Meidam,³⁷ A. Melatos,⁹⁹ G. Mendell,⁴⁵ R. A. Mercer,²³ L. Mereni,²² E. L. Merilh,⁴⁵ M. Merzougui,⁶⁵ S. Meshkov,¹ C. Messenger,⁴⁴ C. Messick,⁸⁸ R. Metzdrorff,⁷¹ P. M. Meyers,⁹⁹ H. Miao,¹¹ C. Michel,²² H. Middleton,⁹⁹ E. E. Mikhailov,¹⁵⁶ L. Milano,^{80,5} A. L. Miller,⁴⁸ A. Miller,^{115,32} M. Millhouse,⁵³ J. C. Mills,⁶⁸ M. C. Milovich-Goff,¹¹³ O. Minazzoli,^{65,157} Y. Minenkov,³¹ A. Mishkin,⁴⁸ C. Mishra,¹⁵⁸ T. Mistry,¹¹⁰ S. Mitra,³ V. P. Mitrofanov,⁶² G. Mitselmakher,⁴⁸ R. Mittleman,¹² G. Mo,⁹⁶ D. Moffa,¹¹⁷ K. Mogushi,⁸⁶ S. R. P. Mohapatra,¹² M. Montani,^{72,73} C. J. Moore,¹⁰ D. Moraru,⁴⁵ G. Moreno,⁴⁵ S. Morisaki,⁸³ B. Mours,³³ C. M. Mow-Lowry,¹¹ Arunava Mukherjee,^{8,9} D. Mukherjee,²³ S. Mukherjee,¹⁰⁶ N. Mukund,³ A. Mullavey,⁷ J. Munch,⁵⁵ E. A. Muñoz,⁴² M. Muratore,³⁴ P. G. Murray,⁴⁴ A. Nagar,^{87,159,160} I. Nardecchia,^{30,31} L. Naticchioni,^{115,32} R. K. Nayak,¹⁶¹ J. Neilson,¹¹³ G. Nelemans,^{64,37} T. J. N. Nelson,⁷ M. Nery,^{8,9} A. Neunzert,¹²⁷ K. Y. Ng,¹² S. Ng,⁵⁵ P. Nguyen,⁷⁰ D. Nichols,^{129,37} A. B. Nielsen,⁸ S. Nissanke,^{129,37} A. Nitz,⁸ F. Nocera,²⁸ C. North,⁶⁸ L. K. Nuttall,¹⁵⁴ M. Obergaulinger,²⁰ J. Oberling,⁴⁵ B. D. O'Brien,⁴⁸ G. D. O'Dea,¹¹³ G. H. Oggin,¹⁶² J. J. Oh,¹³⁹ S. H. Oh,¹³⁹ F. Ohme,^{8,9} H. Ohta,⁸³ M. A. Okada,¹³ M. Oliver,¹⁰¹ P. Oppermann,^{8,9} Richard J. Oram,⁷ B. O'Reilly,⁷ R. G. Ormiston,⁴³ L. F. Ortega,⁴⁸ R. O'Shaughnessy,⁵⁸ S. Ossokine,³⁶ D. J. Ottaway,⁵⁵ H. Overmier,⁷ B. J. Owen,⁸⁵ A. E. Pace,⁸⁸ G. Pagano,^{18,19} M. A. Page,⁶³ A. Pai,¹²³ S. A. Pai,⁶¹ J. R. Palamos,⁷⁰ O. Palashov,¹³⁶ C. Palomba,³² A. Pal-Singh,¹⁴¹ Huang-Wei Pan,⁸⁹ B. Pang,⁴⁶ P. T. H. Pang,⁹³ C. Pankow,⁵⁹ F. Pannarale,^{115,32} B. C. Pant,⁶¹ F. Paoletti,¹⁹ A. Paoli,²⁸ A. Parida,³ W. Parker,^{7,155} D. Pascucci,⁴⁴ A. Pasqualetti,²⁸ R. Passaquietti,^{18,19} D. Passuello,¹⁹ M. Patil,¹⁴⁴ B. Patricelli,^{18,19} B. L. Pearlstone,⁴⁴ C. Pedersen,⁶⁸ M. Pedraza,¹ R. Pedurand,^{22,163} A. Pele,⁷ S. Penn,¹⁶⁴ C. J. Perez,⁴⁵ A. Perreca,^{114,98} H. P. Pfeiffer,^{36,91} M. Phelps,^{8,9} K. S. Phukon,³ O. J. Piccinni,^{115,32} M. Pichot,⁶⁵ F. Piergiovanni,^{72,73} G. Pillant,²⁸ L. Pinard,²² M. Pirello,⁴⁵ M. Pitkin,⁴⁴ R. Poggiani,^{18,19} D. Y. T. Pong,⁹³ S. Ponrathnam,³ P. Popolizio,²⁸ E. K. Porter,²⁷ J. Powell,¹⁵³ A. K. Prajapati,¹⁰⁹ J. Prasad,³ K. Prasai,⁴⁹ R. Prasanna,¹³¹ G. Pratten,¹⁰¹ T. Prestegard,²³ S. Privitera,³⁶ G. A. Prodi,^{114,98} L. G. Prokhorov,⁶² O. Puncken,^{8,9} M. Punturo,⁴¹ P. Puppo,³² M. Pürner,³⁶ H. Qi,²³ V. Quetschke,¹⁰⁶ P. J. Quinonez,³⁴ E. A. Quintero,¹ R. Quitzow-James,⁷⁰ F. J. Raab,⁴⁵ H. Radkins,⁴⁵ N. Radulescu,⁶⁵ P. Raffai,¹⁰⁸ S. Raja,⁶¹ C. Rajan,⁶¹ B. Rajbhandari,⁸⁵ M. Rakhmanov,¹⁰⁶ K. E. Ramirez,¹⁰⁶ A. Ramos-Buades,¹⁰¹ Javed Rana,³ K. Rao,⁵⁹ P. Rapagnani,^{115,32} V. Raymond,⁶⁸ M. Razzano,^{18,19} J. Read,²⁶ T. Regimbau,³³ L. Rei,⁶⁰ S. Reid,²⁴ D. H. Reitze,^{1,48} W. Ren,¹⁷ F. Ricci,^{115,32} C. J. Richardson,³⁴ J. W. Richardson,¹ P. M. Ricker,¹⁷ K. Riles,¹²⁷ M. Rizzo,⁵⁹ N. A. Robertson,^{1,44} R. Robie,⁴⁴ F. Robinet,²⁵ A. Rocchi,³¹ L. Rolland,³³ J. G. Rollins,¹ V. J. Roma,⁷⁰ M. Romanelli,⁶⁷ R. Romano,^{4,5} C. L. Romel,⁴⁵ J. H. Romie,⁷ K. Rose,¹¹⁷ D. Rosińska,^{165,54} S. G. Rosofsky,¹⁷ M. P. Ross,¹⁶⁶ S. Rowan,⁴⁴ A. Rüdiger,^{8,9,†} P. Ruggi,²⁸ G. Rutins,¹⁶⁷ K. Ryan,⁴⁵ S. Sachdev,¹ T. Sadecki,⁴⁵ M. Sakellariadou,¹³³ L. Salconi,²⁸ M. Saleem,²⁹ A. Samajdar,³⁷ L. Sammut,⁶ E. J. Sanchez,¹ L. E. Sanchez,¹ N. Sanchis-Gual,²⁰ V. Sandberg,⁴⁵ J. R. Sanders,⁴² K. A. Santiago,³⁵ N. Sarin,⁶ B. Sassolas,²² B. S. Sathyaprakash,^{88,68} P. R. Saulson,⁴² O. Sauter,¹²⁷ R. L. Savage,⁴⁵ P. Schale,⁷⁰ M. Scheel,⁴⁶ J. Scheuer,⁵⁹ P. Schmidt,⁶⁴ R. Schnabel,¹⁴¹ R. M. S. Schofield,⁷⁰ A. Schönbeck,¹⁴¹ E. Schreiber,^{8,9} B. W. Schulte,^{8,9} B. F. Schutz,⁶⁸ S. G. Schwalbe,³⁴ J. Scott,⁴⁴ S. M. Scott,²¹ E. Seidel,¹⁷ D. Sellers,⁷ A. S. Sengupta,¹⁶⁸ N. Sennett,³⁶ D. Sentenac,²⁸ V. Sequino,^{30,31,14} A. Sergeev,¹³⁶ Y. Setyawati,^{8,9} D. A. Shaddock,²¹ T. Shaffer,⁴⁵ M. S. Shariar,⁵⁹ M. B. Shaner,¹¹³ L. Shao,³⁶ P. Sharma,⁶¹ P. Shawhan,⁷⁶ H. Shen,¹⁷ R. Shink,¹⁶⁹ D. H. Shoemaker,¹² D. M. Shoemaker,⁷⁸ S. ShyamSundar,⁶¹ K. Siellez,⁷⁸ M. Sieniawska,⁵⁴ D. Sigg,⁴⁵ A. D. Silva,¹³ L. P. Singer,⁸¹ N. Singh,⁷⁴

A. Singhal,^{14,32} A. M. Sintes,¹⁰¹ S. Sitmukhambetov,¹⁰⁶ V. Skliris,⁶⁸ B. J. J. Slagmolen,²¹ T. J. Slaven-Blair,⁶³ J. R. Smith,²⁶ R. J. E. Smith,⁶ S. Somala,¹⁷⁰ E. J. Son,¹³⁹ B. Sorazu,⁴⁴ F. Sorrentino,⁶⁰ T. Souradeep,³ E. Sowell,⁸⁵ A. P. Spencer,⁴⁴ A. K. Srivastava,¹⁰⁹ V. Srivastava,⁴² K. Staats,⁵⁹ C. Stachie,⁶⁵ M. Standke,^{8,9} D. A. Steer,²⁷ M. Steinke,^{8,9} J. Steinlechner,^{141,44} S. Steinlechner,¹⁴¹ D. Steinmeyer,^{8,9} S. P. Stevenson,¹⁵³ D. Stocks,⁴⁹ R. Stone,¹⁰⁶ D. J. Stops,¹¹ K. A. Strain,⁴⁴ G. Stratta,^{72,73} S. E. Strigin,⁶² A. Strunk,⁴⁵ R. Sturani,¹⁷¹ A. L. Stuver,¹⁷² V. Sudhir,¹² T. Z. Summerscales,¹⁷³ L. Sun,¹ S. Sunil,¹⁰⁹ J. Suresh,³ P. J. Sutton,⁶⁸ B. L. Swinkels,³⁷ M. J. Szczepańczyk,³⁴ M. Tacca,³⁷ S. C. Tait,⁴⁴ C. Talbot,⁶ D. Talukder,⁷⁰ D. B. Tanner,⁴⁸ M. Tápai,¹²⁴ A. Taracchini,³⁶ J. D. Tasson,⁹⁶ R. Taylor,¹ F. Thies,^{8,9} M. Thomas,⁷ P. Thomas,⁴⁵ S. R. Thondapu,⁶¹ K. A. Thorne,⁷ E. Thrane,⁶ Shubhanshu Tiwari,^{114,98} Srishti Tiwari,¹²⁵ V. Tiwari,⁶⁸ K. Toland,⁴⁴ M. Tonelli,^{18,19} Z. Tornasi,⁴⁴ A. Torres-Forné,¹⁷⁴ C. I. Torrie,¹ D. Töyrä,¹¹ F. Travasso,^{28,41} G. Traylor,⁷ M. C. Tringali,⁷⁴ A. Trovato,²⁷ L. Trozzo,^{175,19} R. Trudeau,¹ K. W. Tsang,³⁷ M. Tse,¹² R. Tso,⁴⁶ L. Tsukada,⁸³ D. Tsuna,⁸³ D. Tuyenbayev,¹⁰⁶ K. Ueno,⁸³ D. Ugolini,¹⁷⁶ C. S. Unnikrishnan,¹²⁵ A. L. Urban,² S. A. Usman,⁶⁸ H. Vahlbruch,⁹ G. Vajente,¹ G. Valdes,² N. van Bakel,³⁷ M. van Beuzekom,³⁷ J. F. J. van den Brand,^{75,37} C. Van Den Broeck,^{37,177} D. C. Vander-Hyde,⁴² J. V. van Heijningen,⁶³ L. van der Schaaf,³⁷ A. A. van Veggel,⁴⁴ M. Vardaro,^{51,52} V. Varma,⁴⁶ S. Vass,¹ M. Vasúth,⁴⁷ A. Vecchio,¹¹ G. Vedovato,⁵² J. Veitch,⁴⁴ P. J. Veitch,⁵⁵ K. Venkateswara,¹⁶⁶ G. Venugopalan,¹ D. Verkindt,³³ F. Vetranò,^{72,73} A. Viceré,^{72,73} A. D. Viets,²³ D. J. Vine,¹⁶⁷ J.-Y. Vinet,⁶⁵ S. Vitale,¹² T. Vo,⁴² H. Vocca,^{40,41} C. Vorvick,⁴⁵ S. P. Vyatchanin,⁶² A. R. Wade,¹ L. E. Wade,¹¹⁷ M. Wade,¹¹⁷ R. M. Wald,⁹² R. Walet,³⁷ M. Walker,²⁶ L. Wallace,¹ S. Walsh,²³ G. Wang,^{14,19} H. Wang,¹¹ J. Z. Wang,¹²⁷ W. H. Wang,¹⁰⁶ Y. F. Wang,⁹³ R. L. Ward,²¹ Z. A. Warden,³⁴ J. Warner,⁴⁵ M. Was,³³ J. Watchi,¹⁰² B. Weaver,⁴⁵ L.-W. Wei,^{8,9} M. Weinert,^{8,9} A. J. Weinstein,¹ R. Weiss,¹² F. Wellmann,^{8,9} L. Wen,⁶³ E. K. Wessel,¹⁷ P. Weßels,^{8,9} J. W. Westhouse,³⁴ K. Wette,²¹ J. T. Whelan,⁵⁸ B. F. Whiting,⁴⁸ C. Whittle,¹² D. M. Wilken,^{8,9} D. Williams,⁴⁴ A. R. Williamson,^{129,37} J. L. Willis,¹ B. Willke,^{8,9} M. H. Wimmer,^{8,9} W. Winkler,^{8,9} C. C. Wipf,¹ H. Wittel,^{8,9} G. Woan,⁴⁴ J. Woehler,^{8,9} J. K. Wofford,⁵⁸ J. Worden,⁴⁵ J. L. Wright,⁴⁴ D. S. Wu,^{8,9} D. M. Wysocki,⁵⁸ L. Xiao,¹ H. Yamamoto,¹ C. C. Yancey,⁷⁶ L. Yang,¹¹⁶ M. J. Yap,²¹ M. Yazback,⁴⁸ D. W. Yeeles,⁶⁸ Hang Yu,¹² Haocun Yu,¹² S. H. R. Yuen,⁹³ M. Yvert,³³ A. K. Zadrożny,^{106,143} M. Zanolin,³⁴ T. Zelenova,²⁸ J.-P. Zendri,⁵² M. Zevin,⁵⁹ J. Zhang,⁶³ L. Zhang,¹ T. Zhang,⁴⁴ C. Zhao,⁶³ M. Zhou,⁵⁹ Z. Zhou,⁵⁹ X. J. Zhu,⁶ A. B. Zimmerman,^{77,91} M. E. Zucker,^{1,12} and J. Zweizig¹

(The LIGO Scientific Collaboration and the Virgo Collaboration)

¹LIGO, California Institute of Technology, Pasadena, California 91125, USA

²Louisiana State University, Baton Rouge, Louisiana 70803, USA

³Inter-University Centre for Astronomy and Astrophysics, Pune 411007, India

⁴Università di Salerno, Fisciano, I-84084 Salerno, Italy

⁵INFN, Sezione di Napoli, Complesso Universitario di Monte S. Angelo, I-80126 Napoli, Italy

⁶OzGrav, School of Physics & Astronomy, Monash University, Clayton 3800, Victoria, Australia

⁷LIGO Livingston Observatory, Livingston, Louisiana 70754, USA

⁸Max Planck Institute for Gravitational Physics (Albert Einstein Institute), D-30167 Hannover, Germany

⁹Leibniz Universität Hannover, D-30167 Hannover, Germany

¹⁰University of Cambridge, Cambridge CB2 1TN, United Kingdom

¹¹University of Birmingham, Birmingham B15 2TT, United Kingdom

¹²LIGO, Massachusetts Institute of Technology, Cambridge, Massachusetts 02139, USA

¹³Instituto Nacional de Pesquisas Espaciais, 12227-010 São José dos Campos, São Paulo, Brazil

¹⁴Gran Sasso Science Institute (GSSI), I-67100 L'Aquila, Italy

¹⁵INFN, Laboratori Nazionali del Gran Sasso, I-67100 Assergi, Italy

¹⁶International Centre for Theoretical Sciences, Tata Institute of Fundamental Research, Bengaluru 560089, India

¹⁷NCSA, University of Illinois at Urbana-Champaign, Urbana, Illinois 61801, USA

¹⁸Università di Pisa, I-56127 Pisa, Italy

¹⁹INFN, Sezione di Pisa, I-56127 Pisa, Italy

²⁰Departamento de Astronomía y Astrofísica, Universitat de València, E-46100 Burjassot, València, Spain

²¹OzGrav, Australian National University, Canberra, Australian Capital Territory 0200, Australia

²²Laboratoire des Matériaux Avancés (LMA), CNRS/IN2P3, F-69622 Villeurbanne, France

²³University of Wisconsin-Milwaukee, Milwaukee, Wisconsin 53201, USA

²⁴SUPA, University of Strathclyde, Glasgow G1 1XQ, United Kingdom

²⁵LAL, Univ. Paris-Sud, CNRS/IN2P3, Université Paris-Saclay, F-91898 Orsay, France

²⁶California State University Fullerton, Fullerton, California 92831, USA

- ²⁷*APC, AstroParticule et Cosmologie, Université Paris Diderot, CNRS/IN2P3, CEA/Irfu, Observatoire de Paris, Sorbonne Paris Cité, F-75205 Paris Cedex 13, France*
- ²⁸*European Gravitational Observatory (EGO), I-56021 Cascina, Pisa, Italy*
- ²⁹*Chennai Mathematical Institute, Chennai 603103, India*
- ³⁰*Università di Roma Tor Vergata, I-00133 Roma, Italy*
- ³¹*INFN, Sezione di Roma Tor Vergata, I-00133 Roma, Italy*
- ³²*INFN, Sezione di Roma, I-00185 Roma, Italy*
- ³³*Laboratoire d'Annecy de Physique des Particules (LAPP), Univ. Grenoble Alpes, Université Savoie Mont Blanc, CNRS/IN2P3, F-74941 Annecy, France*
- ³⁴*Embry-Riddle Aeronautical University, Prescott, Arizona 86301, USA*
- ³⁵*Montclair State University, Montclair, New Jersey 07043, USA*
- ³⁶*Max Planck Institute for Gravitational Physics (Albert Einstein Institute), D-14476 Potsdam-Golm, Germany*
- ³⁷*Nikhef, Science Park 105, 1098 XG Amsterdam, The Netherlands*
- ³⁸*Korea Institute of Science and Technology Information, Daejeon 34141, South Korea*
- ³⁹*West Virginia University, Morgantown, West Virginia 26506, USA*
- ⁴⁰*Università di Perugia, I-06123 Perugia, Italy*
- ⁴¹*INFN, Sezione di Perugia, I-06123 Perugia, Italy*
- ⁴²*Syracuse University, Syracuse, New York 13244, USA*
- ⁴³*University of Minnesota, Minneapolis, Minnesota 55455, USA*
- ⁴⁴*SUPA, University of Glasgow, Glasgow G12 8QQ, United Kingdom*
- ⁴⁵*LIGO Hanford Observatory, Richland, Washington 99352, USA*
- ⁴⁶*Caltech CaRT, Pasadena, California 91125, USA*
- ⁴⁷*Wigner RCP, RMKI, H-1121 Budapest, Konkoly Thege Miklós út 29-33, Hungary*
- ⁴⁸*University of Florida, Gainesville, Florida 32611, USA*
- ⁴⁹*Stanford University, Stanford, California 94305, USA*
- ⁵⁰*Università di Camerino, Dipartimento di Fisica, I-62032 Camerino, Italy*
- ⁵¹*Università di Padova, Dipartimento di Fisica e Astronomia, I-35131 Padova, Italy*
- ⁵²*INFN, Sezione di Padova, I-35131 Padova, Italy*
- ⁵³*Montana State University, Bozeman, Montana 59717, USA*
- ⁵⁴*Nicolaus Copernicus Astronomical Center, Polish Academy of Sciences, 00-716, Warsaw, Poland*
- ⁵⁵*OzGrav, University of Adelaide, Adelaide, South Australia 5005, Australia*
- ⁵⁶*Theoretisch-Physikalisches Institut, Friedrich-Schiller-Universität Jena, D-07743 Jena, Germany*
- ⁵⁷*INFN, Sezione di Milano Bicocca, Gruppo Collegato di Parma, I-43124 Parma, Italy*
- ⁵⁸*Rochester Institute of Technology, Rochester, NY 14623, USA*
- ⁵⁹*Center for Interdisciplinary Exploration & Research in Astrophysics (CIERA), Northwestern University, Evanston, IL 60208, USA*
- ⁶⁰*INFN, Sezione di Genova, I-16146 Genova, Italy*
- ⁶¹*RRCAT, Indore, Madhya Pradesh 452013, India*
- ⁶²*Faculty of Physics, Lomonosov Moscow State University, Moscow 119991, Russia*
- ⁶³*OzGrav, University of Western Australia, Crawley, Western Australia 6009, Australia*
- ⁶⁴*Department of Astrophysics/IMAPP, Radboud University Nijmegen, P.O. Box 9010, 6500 GL Nijmegen, The Netherlands*
- ⁶⁵*Artemis, Université Côte d'Azur, Observatoire Côte d'Azur, CNRS, CS 34229, F-06304 Nice Cedex 4, France*
- ⁶⁶*Physik-Institut, University of Zurich, Winterthurerstrasse 190, 8057 Zurich, Switzerland*
- ⁶⁷*Univ Rennes, CNRS, Institut FOTON—UMR6082, F-3500 Rennes, France*
- ⁶⁸*Cardiff University, Cardiff CF24 3AA, United Kingdom*
- ⁶⁹*Washington State University, Pullman, Washington 99164, USA*
- ⁷⁰*University of Oregon, Eugene, Oregon 97403, USA*
- ⁷¹*Laboratoire Kastler Brossel, Sorbonne Université, CNRS, ENS-Université PSL, Collège de France, F-75005 Paris, France*
- ⁷²*Università degli Studi di Urbino 'Carlo Bo,' I-61029 Urbino, Italy*
- ⁷³*INFN, Sezione di Firenze, I-50019 Sesto Fiorentino, Firenze, Italy*
- ⁷⁴*Astronomical Observatory Warsaw University, 00-478 Warsaw, Poland*
- ⁷⁵*VU University Amsterdam, 1081 HV Amsterdam, The Netherlands*
- ⁷⁶*University of Maryland, College Park, Maryland 20742, USA*
- ⁷⁷*Department of Physics, University of Texas, Austin, Texas 78712, USA*
- ⁷⁸*School of Physics, Georgia Institute of Technology, Atlanta, Georgia 30332, USA*
- ⁷⁹*Université Claude Bernard Lyon 1, F-69622 Villeurbanne, France*

- ⁸⁰*Università di Napoli 'Federico II,' Complesso Universitario di Monte S. Angelo, I-80126 Napoli, Italy*
- ⁸¹*NASA Goddard Space Flight Center, Greenbelt, Maryland 20771, USA*
- ⁸²*Dipartimento di Fisica, Università degli Studi di Genova, I-16146 Genova, Italy*
- ⁸³*RESCEU, University of Tokyo, Tokyo, 113-0033, Japan*
- ⁸⁴*Tsinghua University, Beijing 100084, China*
- ⁸⁵*Texas Tech University, Lubbock, Texas 79409, USA*
- ⁸⁶*The University of Mississippi, University, Mississippi 38677, USA*
- ⁸⁷*Museo Storico della Fisica e Centro Studi e Ricerche "Enrico Fermi", I-00184 Roma, Italy*
- ⁸⁸*The Pennsylvania State University, University Park, Pennsylvania 16802, USA*
- ⁸⁹*National Tsing Hua University, Hsinchu City, 30013 Taiwan, Republic of China*
- ⁹⁰*Charles Sturt University, Wagga Wagga, New South Wales 2678, Australia*
- ⁹¹*Canadian Institute for Theoretical Astrophysics, University of Toronto, Toronto, Ontario M5S 3H8, Canada*
- ⁹²*University of Chicago, Chicago, Illinois 60637, USA*
- ⁹³*The Chinese University of Hong Kong, Shatin, NT, Hong Kong*
- ⁹⁴*Seoul National University, Seoul 08826, South Korea*
- ⁹⁵*Pusan National University, Busan 46241, South Korea*
- ⁹⁶*Carleton College, Northfield, Minnesota 55057, USA*
- ⁹⁷*INAF, Osservatorio Astronomico di Padova, I-35122 Padova, Italy*
- ⁹⁸*INFN, Trento Institute for Fundamental Physics and Applications, I-38123 Povo, Trento, Italy*
- ⁹⁹*OzGrav, University of Melbourne, Parkville, Victoria 3010, Australia*
- ¹⁰⁰*Columbia University, New York, New York 10027, USA*
- ¹⁰¹*Universitat de les Illes Balears, IAC3—IEEC, E-07122 Palma de Mallorca, Spain*
- ¹⁰²*Université Libre de Bruxelles, Brussels 1050, Belgium*
- ¹⁰³*Sonoma State University, Rohnert Park, California 94928, USA*
- ¹⁰⁴*Departamento de Matemáticas, Universitat de València, E-46100 Burjassot, València, Spain*
- ¹⁰⁵*University of Rhode Island, Kingston, Rhode Island 02881, USA*
- ¹⁰⁶*The University of Texas Rio Grande Valley, Brownsville, Texas 78520, USA*
- ¹⁰⁷*Bellevue College, Bellevue, Washington 98007, USA*
- ¹⁰⁸*MTA-ELTE Astrophysics Research Group, Institute of Physics, Eötvös University, Budapest 1117, Hungary*
- ¹⁰⁹*Institute for Plasma Research, Bhat, Gandhinagar 382428, India*
- ¹¹⁰*The University of Sheffield, Sheffield S10 2TN, United Kingdom*
- ¹¹¹*IGFAE, Campus Sur, Universidade de Santiago de Compostela, 15782 Spain*
- ¹¹²*Dipartimento di Scienze Matematiche, Fisiche e Informatiche, Università di Parma, I-43124 Parma, Italy*
- ¹¹³*California State University, Los Angeles, 5151 State University Dr, Los Angeles, California 90032, USA*
- ¹¹⁴*Università di Trento, Dipartimento di Fisica, I-38123 Povo, Trento, Italy*
- ¹¹⁵*Università di Roma 'La Sapienza,' I-00185 Roma, Italy*
- ¹¹⁶*Colorado State University, Fort Collins, Colorado 80523, USA*
- ¹¹⁷*Kenyon College, Gambier, Ohio 43022, USA*
- ¹¹⁸*Christopher Newport University, Newport News, Virginia 23606, USA*
- ¹¹⁹*National Astronomical Observatory of Japan, 2-21-1 Osawa, Mitaka, Tokyo 181-8588, Japan*
- ¹²⁰*Observatori Astronòmic, Universitat de València, E-46980 Paterna, València, Spain*
- ¹²¹*School of Mathematics, University of Edinburgh, Edinburgh EH9 3FD, United Kingdom*
- ¹²²*Institute Of Advanced Research, Gandhinagar 382426, India*
- ¹²³*Indian Institute of Technology Bombay, Powai, Mumbai 400 076, India*
- ¹²⁴*University of Szeged, Dóm tér 9, Szeged 6720, Hungary*
- ¹²⁵*Tata Institute of Fundamental Research, Mumbai 400005, India*
- ¹²⁶*INAF, Osservatorio Astronomico di Capodimonte, I-80131, Napoli, Italy*
- ¹²⁷*University of Michigan, Ann Arbor, Michigan 48109, USA*
- ¹²⁸*American University, Washington, D.C. 20016, USA*
- ¹²⁹*GRAPPA, Anton Pannekoek Institute for Astronomy and Institute of High-Energy Physics, University of Amsterdam, Science Park 904, 1098 XH Amsterdam, The Netherlands*
- ¹³⁰*Delta Institute for Theoretical Physics, Science Park 904, 1090 GL Amsterdam, The Netherlands*
- ¹³¹*Directorate of Construction, Services & Estate Management, Mumbai 400094 India*
- ¹³²*University of Białystok, 15-424 Białystok, Poland*
- ¹³³*King's College London, University of London, London WC2R 2LS, United Kingdom*
- ¹³⁴*University of Southampton, Southampton SO17 1BJ, United Kingdom*

- ¹³⁵*University of Washington Bothell, Bothell, Washington 98011, USA*
¹³⁶*Institute of Applied Physics, Nizhny Novgorod, 603950, Russia*
¹³⁷*Ewha Womans University, Seoul 03760, South Korea*
¹³⁸*Inje University Gimhae, South Gyeongsang 50834, South Korea*
¹³⁹*National Institute for Mathematical Sciences, Daejeon 34047, South Korea*
¹⁴⁰*Ulsan National Institute of Science and Technology, Ulsan 44919, South Korea*
¹⁴¹*Universität Hamburg, D-22761 Hamburg, Germany*
¹⁴²*Maastricht University, P.O. Box 616, 6200 MD Maastricht, The Netherlands*
¹⁴³*NCBJ, 05-400 Świerk-Otwock, Poland*
¹⁴⁴*Institute of Mathematics, Polish Academy of Sciences, 00656 Warsaw, Poland*
¹⁴⁵*Cornell University, Ithaca, New York 14850, USA*
¹⁴⁶*Hillsdale College, Hillsdale, Michigan 49242, USA*
¹⁴⁷*Hanyang University, Seoul 04763, South Korea*
¹⁴⁸*Korea Astronomy and Space Science Institute, Daejeon 34055, South Korea*
¹⁴⁹*NASA Marshall Space Flight Center, Huntsville, Alabama 35811, USA*
¹⁵⁰*Dipartimento di Matematica e Fisica, Università degli Studi Roma Tre, I-00146 Roma, Italy*
¹⁵¹*INFN, Sezione di Roma Tre, I-00146 Roma, Italy*
¹⁵²*ESPCI, CNRS, F-75005 Paris, France*
¹⁵³*OzGrav, Swinburne University of Technology, Hawthorn VIC 3122, Australia*
¹⁵⁴*University of Portsmouth, Portsmouth, PO1 3FX, United Kingdom*
¹⁵⁵*Southern University and A&M College, Baton Rouge, Louisiana 70813, USA*
¹⁵⁶*College of William and Mary, Williamsburg, Virginia 23187, USA*
¹⁵⁷*Centre Scientifique de Monaco, 8 quai Antoine 1er, MC-98000, Monaco*
¹⁵⁸*Indian Institute of Technology Madras, Chennai 600036, India*
¹⁵⁹*INFN Sezione di Torino, Via P. Giuria 1, I-10125 Torino, Italy*
¹⁶⁰*Institut des Hautes Etudes Scientifiques, F-91440 Bures-sur-Yvette, France*
¹⁶¹*IISER-Kolkata, Mohanpur, West Bengal 741252, India*
¹⁶²*Whitman College, 345 Boyer Avenue, Walla Walla, Washington 99362 USA*
¹⁶³*Université de Lyon, F-69361 Lyon, France*
¹⁶⁴*Hobart and William Smith Colleges, Geneva, New York 14456, USA*
¹⁶⁵*Janusz Gil Institute of Astronomy, University of Zielona Góra, 65-265 Zielona Góra, Poland*
¹⁶⁶*University of Washington, Seattle, Washington 98195, USA*
¹⁶⁷*SUPA, University of the West of Scotland, Paisley PA1 2BE, United Kingdom*
¹⁶⁸*Indian Institute of Technology, Gandhinagar Ahmedabad Gujarat 382424, India*
¹⁶⁹*Université de Montréal/Polytechnique, Montreal, Quebec H3T 1J4, Canada*
¹⁷⁰*Indian Institute of Technology Hyderabad, Sangareddy, Khandi, Telangana 502285, India*
¹⁷¹*International Institute of Physics, Universidade Federal do Rio Grande do Norte, Natal RN 59078-970, Brazil*
¹⁷²*Villanova University, 800 Lancaster Ave, Villanova, Pennsylvania 19085, USA*
¹⁷³*Andrews University, Berrien Springs, Michigan 49104, USA*
¹⁷⁴*Max Planck Institute for Gravitationalphysik (Albert Einstein Institute), D-14476 Potsdam-Golm, Germany*
¹⁷⁵*Università di Siena, I-53100 Siena, Italy*
¹⁷⁶*Trinity University, San Antonio, Texas 78212, USA*
¹⁷⁷*Van Swinderen Institute for Particle Physics and Gravity, University of Groningen, Nijenborgh 4, 9747 AG Groningen, The Netherlands*

[†]Deceased.